JEM Journal of Experimental Medicine

ARTICLE

MCRS1 sensitizes T cell–dependent immunotherapy by augmenting MHC-I expression in solid tumors

Xue Li[1*], Han Yi[1*], Zheyu Jin[1*], Kaitao Jiang[1*], Kangkang Xue[1], Jin Wang[2], Yuping Qian[2], Qian Xiang[3], Sijing Zhu[1], Runhe Yan[1], Yulong Yang[2], Shenfei Sun[4], Kai Li[1,5], Zichu Zhou[1], Wei Yu[1], Ning Jiang[1], Chen Ding[1,5], Xinhua Lin[4], Jiang Zhong[1], Yuchao Dong[3], Yanfang Liu[2,6], and Xiaofei Yu[1,7]

Dampened antigen presentation underscores the resistance of pancreatic cancer to T cell–mediated anti-tumor immunity, rendering immunotherapy largely ineffective. By high-throughput CRISPR activation perturbation, we discovered that the transcriptional regulator MCRS1 significantly augmented the sensitivity of mouse pancreatic cancer cells to T cell immunity in vitro and in vivo. Mechanistically, MCRS1 interacted with the transcription factor and genome organizer YY1 to coordinately increase the chromatin accessibility and expression of MHC-I genes. Elevated MCRS1 subverted MHC-I suppression and activated anti-tumor T cells, which sensitized mouse pancreatic cancer to α-PD-1 therapy. Remarkably, high MCRS1 expression was associated with increased T cell infiltration and extended survival of patients with pancreatic cancer and was predictive of favorable responses to α-PD-1 therapy in patients with lung cancer. Together, our study uncovers that MCRS1 sensitizes cancer cells to T cell immunity by transcriptionally subverting MHC-I suppression, which enhances the effectiveness of α-PD-1 therapy in mice and humans, paving the way to further improve immunotherapy against solid tumors.

Introduction

T cell immunity is the body's crucial surveillance mechanism against cancerous cells, which underpins the success of newly emerged immunotherapy and contributes to the effectiveness of conventional chemotherapy and radiotherapy (Gotwals et al., 2017; Metcalf et al., 2021; Wang et al., 2024). Cancer cells have devised various strategies to evade T cell–mediated anti-tumor immunity (Mellman et al., 2023), including reducing tumor recognition by dampening antigen presentation and suppressing T cell responses by creating an immune inhibitory tumor microenvironment. These evasion mechanisms collectively render cancer cells insensitive to T cell immunity in solid tumors, representing a significant challenge for immunotherapy such as PD-1 blockade. Therefore, identifying factors that can sensitize or predict T cell responses against solid tumors would pave the way to further improve the efficacies of cancer treatment.

Tumor recognition is a prerequisite for T cell–mediated anti-tumor immunity and critically depends upon tumor antigens presented by the major histocompatibility complex (MHC)-I (Waldman et al., 2020). Once primed by antigen-presenting cells, cytotoxic effector T cells can recognize tumor antigens presented by MHC-I on the tumor cell surface, resulting in antigen-dependent killing of tumor cells. Unsurprisingly, cancer cells could actively suppress antigen presentation by inducing MHC-I degradation and downregulating or mutating genes involved in MHC-I–mediated antigen presentation (Gettinger et al., 2017; Yamamoto et al., 2020b). Indeed, effective immunotherapy, such as immune checkpoint blockade (ICB), relies on the pre-existing T cell immunity in the tumor (Galon and Bruni, 2019), reinforcing the importance of antigen presentation and tumor recognition. Concordantly, targeting the MHC-I degradation pathways has been found to augment antigen presentation and sensitize tumor clearing by T cells in multiple tumor models (Chen et al., 2023; Liu et al., 2020; Yamamoto et al., 2020b). However, this approach could be limited by the expression suppression of the MHC-I machinery in some cancers, and complementary strategies to elevate basal MHC-I expression may further sensitize cancer cells to T cell–mediated anti-tumor immunity.

Pancreatic cancer exhibits the highest mortality rate of all major cancers (Johnson et al., 2017; Siegel et al., 2022), partially

[1]State Key Laboratory of Genetic Engineering, School of Life Sciences, Fudan University, Shanghai, China; [2]Department of Pathology, Changhai Hospital, Naval Medical University, Shanghai, China; [3]Department of Respiratory and Critical Care Medicine, Changhai Hospital, Naval Medical University, Shanghai, China; [4]Zhongshan Hospital, Greater Bay Area Institute of Precision Medicine (Guangzhou), Fudan University, Shanghai, China; [5]Institutes of Biomedical Sciences, Human Phenome Institute, Fudan University, Shanghai, China; [6]National Key Laboratory of Immunity and Inflammation, Institute of Immunology, Naval Medical University, Shanghai, China; [7]Fudan Zhangjiang Institute, Shanghai, China.

*X. Li, H. Yi, Z. Jin, and K. Jiang contributed equally to this paper. Correspondence to Xiaofei Yu: xiaofei_yu@fudan.edu.cn; Yanfang Liu: liuyanfang00215@163.com.

due to resistance to traditional treatment and immunotherapy. Pancreatic cancer cells bear lower mutational loads than other tumor types and actively suppress antigen presentation by inducing MHC-I degradation (Maleki Vareki, 2018; Yamamoto et al., 2020a, 2020b; Zhong et al., 2020). The lack of immune recognition, together with the strong immune-suppressive microenvironment (Ho et al., 2020; Schumacher and Schreiber, 2015), underscores the immunological "coldness" of pancreatic cancer and consequent immune evasion. Indeed, reinvigorating T cells by immunotherapy, such as ICB, fails to elicit meaningful immune responses against pancreatic cancer (Mellman et al., 2011; Waldman et al., 2020). Conversely, inhibiting MHC-I degradation by autophagy has been shown to enhance T cell response against pancreatic tumors in mice (Yamamoto et al., 2020a, 2020b). Furthermore, long-term survivors of pancreatic ductal adenocarcinoma (PDAC), the most common type of pancreatic cancer, have been found to exhibit spontaneous T cell responses against tumor antigens (Balachandran et al., 2017; Łuksza et al., 2022). These data suggest that sensitizing pancreatic cancer to T cell immunity may yield clinical benefits in patients.

To identify new immune-sensitizing pathways in pancreatic cancer, we set up an in vitro syngenic tumor-CD8$^+$ T cell coculture system (Joung et al., 2022; Kearney et al., 2018; Patel et al., 2017), which allowed direct evaluation of cancer immune sensitivity using effector T cell–mediated killing as a readout. We further coupled this system with CRISPRa-mediated gene activation to simultaneously interrogate the functions of thousands of genes while minimizing potentially functional redundancy commonly associated with loss-of-function screening (Chavez et al., 2015; Gilbert et al., 2014; Horlbeck et al., 2016). By doing so, we identified MCRS1 (*Microspherule protein 1*) as a critical immune-sensitizing factor to enhance T cell infiltration and improve the efficacy of α-PD-1 therapy. Given the technological advances in gene delivery and drug-induced gene activation (Gourisankar et al., 2023), MCRS1 may serve as a therapeutic target to sensitize cancer cells to T cell immunity and improve the efficacy of immunotherapy.

Results

Focused CRISPRa screening identifies *Mcrs1* as a potent immune-sensitizing factor in pancreatic cancer

To identify immune-sensitizing factors in pancreatic cancer, we took advantage of a mouse PDAC cell line, HT, which was derived from the spontaneous tumor of a *p48Cre*; *LSL-Kras^{G12D}*; *p53$^{L/+}$* mouse with a C57BL/6 background. The HT cells thus harbored the most frequent human PDAC driver mutations and allowed proper recognition and response by the immune system in congenic mice. Indeed, orthotopic implantation of HT cells into the pancreas of WT mice resulted in the outgrowth of tumors that exhibited the histological and immunological features of human PDAC tumors (Fig. S1, A and B), including atypical tubular structures, activation of stromal cells (α-smooth muscle actin, αSMA$^+$) and a barricade of immune infiltration. As mouse pancreatic cancer cells could be variable in immunogenicity (Li et al., 2018), we also inoculated HT cells subcutaneously into WT and T cell–deficient *Tcrb$^{-/-}$;Tcrd$^{-/-}$* mice and found that tumors showed similar growth dynamics in the two groups of mice (Fig. S1, C and D). These data suggested that HT cells were poorly immunogenic, mirroring the key feature of human PDAC.

We then engineered HT cells to stably express the nuclease-null *Cas9* fused with VP64-p65-Rta domains (*dCas9-VPR*) (Fig. S1 E), which permitted high-throughput activation of single guide RNA (sgRNA)–targeted genes (Chavez et al., 2015; Ho et al., 2020). A single clone was selected based on the cistronic expression of near-infrared fluorescent protein (iRFP) for further studies (HT^{dCas9VPR}, Fig. S1 F). To test whether this system was functional, we transduced the HT^{dCas9VPR} cells with sgRNAs targeting *Leptin*, a gene specifically expressed by adipocytes (Friedman, 2019). *Leptin* expression was highly induced (~200 folds) by sgRNA (Fig. S1 G), suggesting that the *dCas9-VPR*–based CRISPRa system could efficiently activate sgRNA-target genes in the mouse pancreatic cancer cells.

Transcriptional programming dictates key steps of animal development and tumorigenesis (Hanahan and Weinberg, 2011; Joung et al., 2023). We thus sought to screen transcriptional regulators to identify factors that could potentially sensitize pancreatic cancer cells to T cell immunity (Fig. 1 A). To this end, we transduced HT^{dCas9VPR} cells with an experimentally verified CRISPR activation (CRISPRa) sgRNA library that included 10,080 sgRNAs targeting 2,016 transcriptional regulators and 250 non-targeting, negative control sgRNAs (Horlbeck et al., 2016). sgRNA-positive cells were then pulse-loaded with a MHC-I–restricted model antigen, hgp100, which could be specifically recognized by CD8$^+$ T cells expressing the cognate *Pmel-1* T cell receptor (TCR) (Overwijk et al., 1998). Co-culturing of hgp100-loaded tumor cells with *Pmel-1* CD8$^+$ T cells would mimic the effector T cell–tumor interaction at the tumor sites and result in antigen-dependent killing of tumor cells by T cells (the "killing" group), with immune-sensitized tumor cells disproportionally depleted (Fig. 1 A). To rule out antigen-independent effects, we omitted hgp100 from the same tumor–T cell coculture as a control (the "mock" group). After three rounds of iterative screening, we detected clear distinctions between the sgRNA pools of the killing and mock groups (Fig. S1 H), indicating that CRISPRa activation of transcriptional regulators altered the sensitivity of tumor cells to T cell immunity.

We then sought to identify immune-sensitizing factors by prioritizing genes according to changes in sgRNA abundance with two independent analysis algorithms, MAGeCK and ScreenProcessing (Horlbeck et al., 2016; Li et al., 2014) (Fig. S1, I and J). With the MAGeCK analysis pipeline (Li et al., 2014), we found *Pitx1* among the top enriched genes in the killing group (Fig. S1 I), which has been shown to suppress type I interferon signaling and the immune regulators IRF3 and IRF7 that are critical for T cell–mediated anti-tumor immunity (Island et al., 2002). Conversely, *Dusp5* was among the most depleted genes, which is a negative regulator of *Kras* signaling and has been shown to suppress *Kras^{G12D}*-driven PDAC progression in vivo (Kidger et al., 2022). While ScreenProcessing yielded fewer hits (Fig. S1 J), both algorithms identified *Mcrs1*, *Zfp385b*, and *Pcdh1* as significantly depleted genes in the killing group (Fig. 1 B).

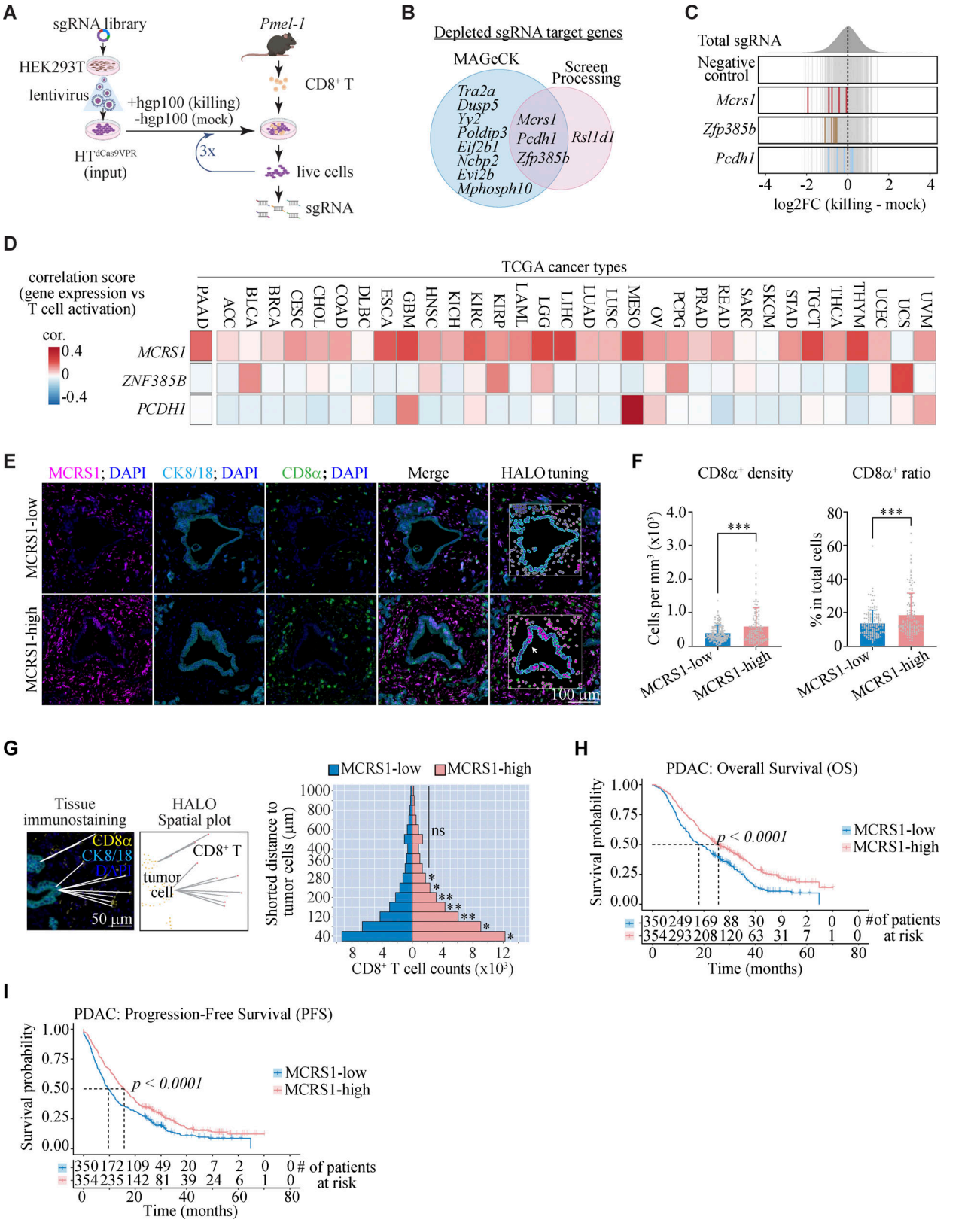

Figure 1. **Focused CRISPRa screening identifies *Mcrs1* as a potential immune-sensitizing factor. (A)** Screening strategy. The mouse pancreatic cancer cell line HT was transduced with a CRISPRa library, followed by hgp100 antigen loading and incubation with *Pmel-1* CD8⁺ effector T cells. sgRNAs in surviving cells after three rounds of T cell killing were profiled by deep sequencing (n = 3 biological replicates for all groups). Illustration was created with https://BioRender.com with modifications. **(B)** Overlapping genes identified by MAGeCK and ScreenProcessing analysis. **(C)** Log_2 fold changes of sgRNAs for candidate genes between the killing condition and the mock condition. **(D)** Correlation between the expression of candidate genes and a predefined T cell activation signature in

patient tumor samples from The Cancer Genome Atlas (TCGA). ACC, adrenocortical carcinoma; BLCA, bladder urothelial carcinoma; BRCA, breast invasive carcinoma; CESC, cervical squamous cell carcinoma and endocervical adenocarcinoma; CHOL, cholangio carcinoma; COAD, colon adenocarcinoma; DLBC, lymphoid neoplasm diffuse large b-cell lymphoma; ESCA, esophageal carcinoma; GBM, glioblastoma multiforme; HNSC, head and neck squamous cell carcinoma; KICH, kidney chromophobe; KIRC, kidney renal clear cell carcinoma; KIRP, kidney renal papillary cell carcinoma; LAML, acute myeloid leukemia; LGG, brain lower grade glioma; LIHC, liver hepatocellular carcinoma; LUAD, lung adenocarcinoma; LUSC, lung squamous cell carcinoma; MESO, mesothelioma; OV, ovarian serous cystadenocarcinoma; PAAD, pancreatic adenocarcinoma; PCPG, pheochromocytoma and paraganglioma; PRAD, prostate adenocarcinoma; READ, rectum adenocarcinoma; SARC, sarcoma; SKCM, skin cutaneous melanoma; STAD, stomach adenocarcinoma; TGCT, testicular germ cell tumors; THCA, thyroid carcinoma; THYM, thymoma; UCEC, uterine corpus endometrial carcinoma; UCS, uterine carcinosarcoma; UVM,uveal melanoma. **(E)** Representative images of immunofluorescence staining of MCRS1 (magenta) in human PDAC samples, together with DAPI (blue, DNA), CK8/18 (cyan, tumor), and CD8α (green, T cell). MCRS1 expression in PDAC cells was quantified and shown in the HALO tuning image (n = 5 for both groups). Scale bar = 100 µm. **(F)** CD8α$^+$ T cell densities and frequencies in human PDAC samples (n = 142, 121 for the MCRS1-low and MCRS1-high groups, respectively; presented as means ± SDs; ***, P < 0.001; two-tailed unpaired t test). **(G)** The shortest distances between CD8α$^+$ T cells and tumor cells in PDAC samples determined with HALO software. Left, representative image for analysis, scale bar = 50 µm. Right, the spatial distribution of CD8α$^+$ T cells plotted for PDAC samples with high and low MCRS1 levels (n = 142, 121 for the MCRS1-low and MCRS1-high groups, respectively; ns, not significant, P ≥ 0.05; *, P < 0.05; **, P < 0.01; two-tailed unpaired t test). **(H)** Overall survival of PDAC patients with high and low MCRS1 levels (n = 350, 354 for the MCRS1-low and MCRS1-high groups, respectively; Kaplan–Meier test). **(I)** Progression-free survival of PDAC patients with high and low MCRS1 levels (n = 350, 354 for the MCRS1-low and MCRS1-high groups, respectively; Kaplan–Meier test).

Inspection of individual sgRNAs targeting the three genes confirmed their depletion in the killing group (Fig. 1 C), indicating that activation of *Mcrs1*, *Zfp385b*, and *Pcdh1* expression might sensitize pancreatic cancer cells to T cell immunity.

To reveal the clinical relevance of our screen candidates, we analyzed the correlation between candidate gene expression and T cell activation in pancreatic cancer (PAAD, pancreatic adenocarcinoma) with the RNA sequencing (RNA-seq) data of The Cancer Genome Atlas (TCGA) (Fig. 1 D). We found that *MCRS1* expression was positively correlated with a T cell activation signature in pancreatic cancer (Singer et al., 2016), in line with our screen setup. In contrast, no significant correlation was detected for *ZNF385B* or *PCDH1*. Remarkably, the positive correlation between *MCRS1* expression and T cell activation could be observed in the majority (28 out 33) of TCGA tumor types, suggesting that *MCRS1* might regulate a pivotal immune-sensitizing pathway in cancer cells and that activation of *MCRS1* expression might yield therapeutic benefits for a wide range of cancer types.

To examine detailed *MCRS1* expression patterns in PDAC, we collected PDAC surgical samples from 704 patients at different disease stages (Table S1) and examined MCRS1 expression by immunohistochemistry (IHC) (Fig. S1 K). We found that MCRS1 levels were significantly lower in poorly differentiated tumors (histological grade III) (Fig. S1, L and M) and in advanced-stage tumors (Fig. S1, N and O). Consistent with RNA-seq analysis of the TCGA dataset, we found that MCRS1-high tumors displayed increased CD8$^+$ T cell infiltration compared to MCRS1-low tumors (Fig. 1, E and F). This was further supported by the shorter distances between CD8$^+$ T cells and the malignant ductal epithelial cells in MCRS1-high tumors than in MCRS1-low tumors (Fig. 1 G). Critically, patients with high MCRS1 expression exhibited significantly longer overall survival and progression-free survival than those with low MCRS1 expression (Fig. 1, H and I).

Taken together, our data showed that high *Mcrs1* expression sensitized mouse pancreatic cancer cells to T cell immunity and was associated with increased CD8$^+$ T infiltration and improved survival of PDAC patients. This suggested that *Mcrs1* could be a crucial enabler of T cell–mediated anti-tumor immunity in pancreatic cancer. We next sought to investigate the mechanism by which MCRS1 regulates the tumor–T cell interaction.

MCRS1 suppresses pancreatic cancer growth in a T cell–dependent manner

Mcrs1, also known as *Microspherule protein 1*, is highly conserved from zebrafish to humans, but its molecular function is not yet well understood (Huang et al., 2022). Interestingly, *MCRS1* expression in the pancreas is among the lowest in normal human tissues and is upregulated in pancreatic cancer (Huang et al., 2022), indicating *MCRS1* might be induced as a cell-intrinsic defense mechanism against tumorigenesis. To elucidate the role of *Mcrs1* in pancreatic cancer, we elevated *Mcrs1* expression in HT cells by lentivirus-mediated overexpression of FLAG-fused mouse *Mcrs1* (*Mcrs1*^{OX}). This could serve as a complementary approach to CRISPRa, as a recent study has revealed that CRISPRa and open reading frame (ORF) overexpression may elicit different biological effects (Joung et al., 2023). Critically, *Mcrs1*^{OX} cells showed increased *Mcrs1* mRNA and protein levels compared to vector control cells (vector), with the fold of increase comparable to that observed between *MCRS1*-high and -low tumors in the TCGA PAAD cohort (Fig. S2, A–C). Of note, elevated *Mcrs1* did not cause significant changes in cell proliferation or cell cycle progression (Fig. S2, D and E).

To confirm the immune-sensitizing effect of *Mcrs1* observed in our CRSPRa screening, we performed in vitro cytotoxicity assays with *Pmel-1* CD8$^+$ T cells across a wide range of effector (T cells): target (cancer cells) ratios. To further increase the robustness of our findings, we also employed a complementary model antigen-TCR system by loading tumor cells with the SIINFEKL octapeptide (OVA) from chicken *Ovalbumin*, which could be recognized by CD8$^+$ T cells expressing the cognate OT-I TCR (Rotzschke et al., 1991). By mixing vector control and *Mcrs1*^{OX} in the co-culture with *Pmel-1* or OT-I CD8$^+$ T cells, we found that *Mcrs1*^{OX} cells were preferentially depleted by T cells (Fig. 2 A). When separately incubated with T cells, fewer *Mcrs1*^{OX} cells survived than vector control cells (Fig. 2 B) while eliciting stronger IFN-γ production by T cells (Fig. 2 C). Together, by using complementary experimental settings, our data showed that elevated *Mcrs1* expression sensitized pancreatic cancer cells

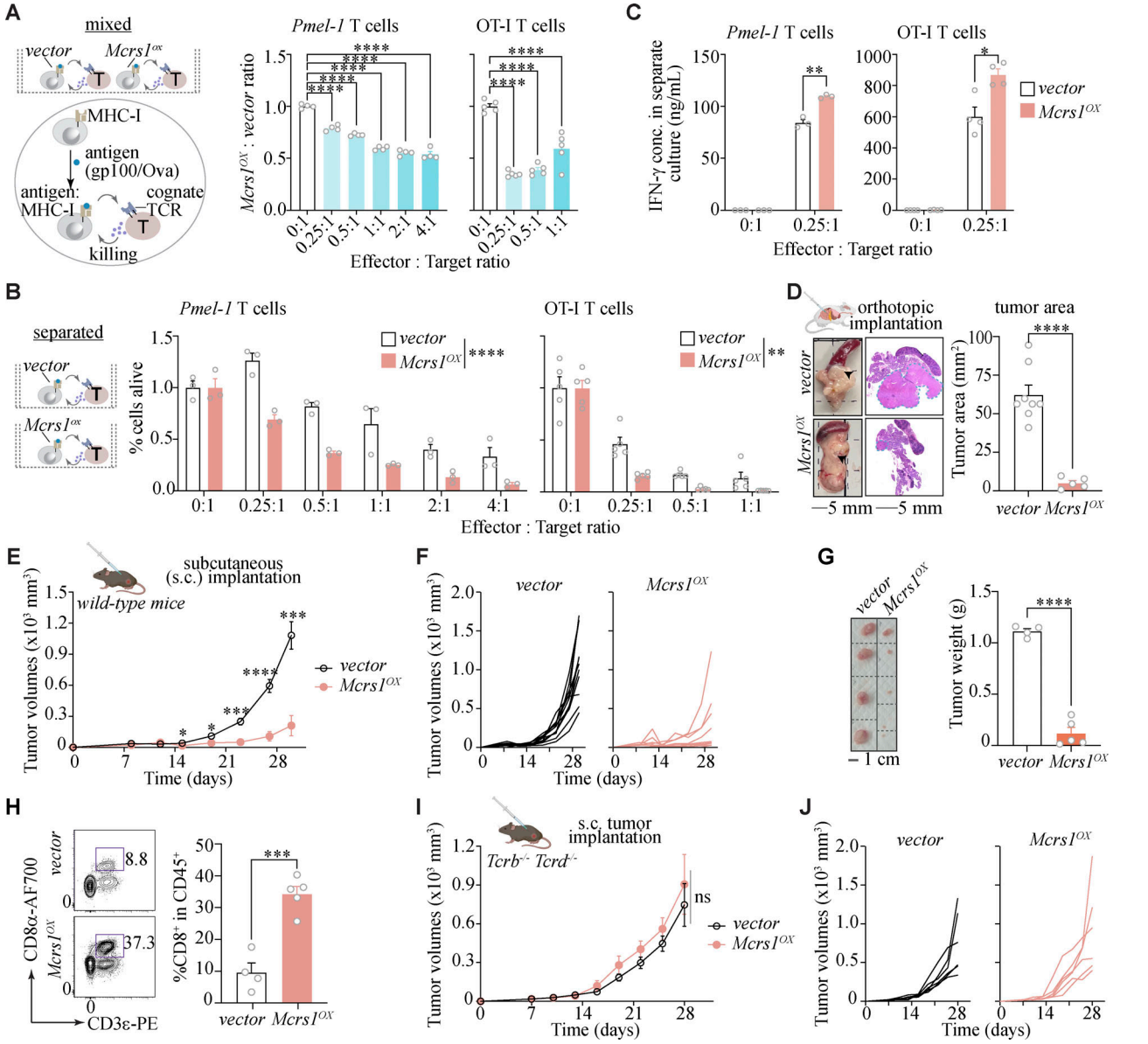

Figure 2. ***Mcrs1* suppresses mouse pancreatic cancer growth in a T cell–dependent manner. (A)** In vitro cytotoxicity assays for the mixed culture of vector control and *Mcrs1*^{OX} cells. *Mcrs1*^{OX} or vector control cells were differentially labeled with the CellTrace Violet dye and loaded with antigen peptides, followed by incubation with CD8$^+$ effector T cells with cognate TCRs at different effector:target ratios. The ratio between live *Mcrs1*^{OX} and vector control cells (7-AAD$^-$) after T cell killing was quantified by flow cytometry (n = 4, 5 for *Pmel-1* and OT-I assays, respectively; presented as means ± SEM; ****, P < 0.0001; one-way ANOVA with Dunnett's multiple comparisons test; N = 2 independent experiments). **(B)** In vitro cytotoxicity assays for vector control and *Mcrs1*^{OX} cells cultured separately. *Mcrs1*^{OX} or vector control cells were loaded with the antigen peptides and separately incubated with CD8$^+$ effector T cells with cognate TCRs at different effector:target ratios. Live cells were determined by flow cytometry (7-AAD$^-$), quantified with CountBright beads, and normalized against the cancer cell-only group (effector:target = 0:1) (n = 3, 5 for *Pmel-1* and OT-I assays, respectively; presented as means ± SEM; **, P < 0.01; ****, P < 0.0001; two-way ANOVA; N = 2 independent experiments). **(C)** IFN-γ concentrations in the supernatant of the in vitro cytotoxicity assays as described in B with an effector:target ratio of 0.25:1. (n = 3, 4 for *Pmel-1* and OT-I assays, respectively; presented as means ± SEM; *, P < 0.05; **, P < 0.01; two-tailed unpaired t test; N = 2 independent experiments). **(D)** Growth of orthotopic tumors in WT mice by injecting *Mcrs1*^{OX} and vector control cells into the pancreas. Shown are representative tumor images with arrowheads indicating tumor masses, H&E staining images, and quantification of tumor areas; scale bars = 5 mm (n = 8, 5 for vector control and *Mcrs1*^{OX}, respectively; presented as means ± SEM; ****, P < 0.0001; two-tailed unpaired t test; N = 3 independent experiments). Illustration was created with https://BioRender.com. **(E)** The growth curve of subcutaneous *Mcrs1*^{OX} and vector control tumors in WT mice (n = 11, 13 for vector control and *Mcrs1*^{OX}, respectively; presented as means ± SEM; *, P < 0.05; ***, P < 0.001; ****, P < 0.0001; two-way ANOVA with Sidak's multiple comparisons test; N > 3 independent experiments). Illustration was created with https://BioRender.com. **(F)** Spider plots showing the growth of individual *Mcrs1*^{OX} and vector control tumors in WT mice as in E. **(G)** Tumor weights at the point of sacrifice with a representative image of the tumor masses; scale bar = 1 cm (n = 4, 5 for vector control and *Mcrs1*^{OX}, respectively; presented as means ± SEM; ****, P < 0.0001; two-tailed unpaired t test; N > 3 independent experiments). **(H)** Flow cytometry analysis of CD8$^+$ T cell frequencies in subcutaneous *Mcrs1*^{OX} or vector control tumors (n = 4, 5 for vector control and *Mcrs1*^{OX}, respectively; presented as means ± SEM; ***, P < 0.001; two-tailed unpaired t test; N > 3 independent experiments). **(I)** The growth curve of subcutaneous *Mcrs1*^{OX} and vector control tumors in T cell–deficient *Tcrb*$^{-/-}$;*Tcrd*$^{-/-}$ mice with WT mice obtained from SLAC as control (n = 6 for both groups; presented as means ± SEM; ns, not significant, P ≥ 0.05; two-way ANOVA, N = 2 independent experiments). Illustration was created with https://BioRender.com. **(J)** Spider plots showing the growth of individual subcutaneous *Mcrs1*^{OX} and vector control tumors in *Tcrb*$^{-/-}$;*Tcrd*$^{-/-}$ mice as in I.

to T cell immunity in vitro, consistent with our CRISPRa screening.

We then examined the immune-sensitizing effect of *Mcrs1* in vivo. To this end, we orthotopically grafted *Mcrs1*^{OX} and vector control cells into the pancreas of WT female mice. We found that the growth of *Mcrs1*^{OX} tumors was significantly reduced compared to vector control tumors (Fig. 2 D), in line with our in vitro data. To confirm this finding and conveniently monitor tumor growth, we adopted a subcutaneous tumor model by inoculating *Mcrs1*^{OX} and vector control cells into the flanks of male mice. Unsurprisingly, we found that *Mcrs1*^{OX} tumors grew significantly slower than vector control tumors (Fig. 2, E and F). This was further confirmed by lower weights of *Mcrs1*^{OX} tumors than vector control tumors at the time of sacrifice (Fig. 2 G). These data collectively suggested that elevated *Mcrs1* expression suppressed pancreatic cancer in vivo, irrespective of tissue sites. Of note, as a control, we employed the same test strategy for a less-likely candidate from our screening, *Pcdh1*, but found no effects on tumor growth (Fig. S2, F and G), indicative of a specific effect of *Mcrs1* in tumor suppression.

To test whether *Mcrs1* suppressed tumor growth via immune sensitization, we unbiasedly profiled the immune landscapes in subcutaneous tumors with RNA-seq. In line with reduced tumor growth, *Mcrs1*^{ox} tumors displayed overall activation of anti-tumor immunity (Fig. S2 H), including upregulation of genes involved in T cell functions (*Cd8a*, *Cd8b1*, *Cd3g*, *Cd3e*, and *Tbx21*) and interferon signaling (*Isg15*, *Gbp8*, *Oas2*, and *Oas3*). We then inferred immune cell fractions from whole-tumor transcriptomes with CIBERSORTx (Newman et al., 2019) and detected a significant increase of CD8$^+$ T cells in *Mcrs1*^{OX} tumors compared to control tumors (Fig. S2, I and J). The increased infiltration of CD8$^+$ T cells in *Mcrs1*^{OX} tumors was further confirmed by flow cytometry (Fig. 2 H and Fig. S2 K), consistent with our observation in human PDAC patients (Fig. 1, E–G). A similar increase of CD4$^+$ T cell infiltration could also be observed by flow cytometry analysis (Fig. S2 L).

Lastly, to test whether T cells were responsible for *Mcrs1*-mediated tumor suppression, we grafted *Mcrs1*^{OX} and vector control cells into cogenetic *Tcrb*$^{-/-}$;*Tcrd*$^{-/-}$ mice that were deficient in T cells. In contrast to our observation in WT mice, *Mcrs1*^{OX} tumors grew comparably to vector control tumors in *Tcrb*$^{-/-}$;*Tcrd*$^{-/-}$ mice (Fig. 2, I and J). Together, these data showed that *Mcrs1* suppressed pancreatic tumor growth in a T cell–dependent manner without affecting tumor cell proliferation. Thus, elevated *Mcrs1* expression could sensitize pancreatic cancer cells to T cell–mediated anti-tumor immunity, reverting the immunologic "coldness" typically associated with pancreatic cancer.

Elevated *Mcrs1* expression activates T cell–mediated anti-tumor immunity in vivo

To comprehensively examine the effect of *Mcrs1* on T cells, we isolated tumor-infiltrating lymphocytes (TILs, CD45$^+$ CD90.2$^+$) from control and *Mcrs1*^{OX} tumors and performed single-cell RNA-seq (scRNA-seq) paired with TCR-seq (scTCR-seq) (Stoeckius et al., 2018) (Fig. 3 A). As expected, the majority of captured cells were lymphocytes (Fig. S3 A), which could be computationally clustered into 14 clusters (Fig. 3 A and Fig. S3 B). Each cluster represented a distinct cell type or cell state, with seven clusters representing CD8$^+$ T cells at different functional states from early activation (CD8 T Proliferating) to late activation/exhaustion (CD8 T_{Exh}) and memory formation (T_{EM}), three clusters for CD4$^+$ T cells, two clusters for natural killer (NK) cells, one cluster for NKT cells and one cluster for γδ T cells. In line with increased T cell infiltration (Fig. 2 H and Fig. S2, J and L), we observed apparent expansion of post-activation CD8$^+$ T cells (effector-memory T_{EM}, exhausted T_{Exh}) and type 1 CD4$^+$ cells (T_H1) in *Mcrs1*^{OX} tumors (Fig. 3 B). Accordantly, pseudo-bulk analysis also revealed significant upregulation of post-activation markers in CD8$^+$ and CD4$^+$ T cells, such as *Nr4a2*, *Pdcd1*, *Lag3*, *Vps37b*, and *Ramp3*, in *Mcrs1*^{OX} tumors (Fig. S3 C).

As CD8$^+$ T cells execute the tumor recognition and killing functions in anti-tumor immunity, we wanted to examine the dynamic functional changes of CD8$^+$ T cells in vector control and *Mcrs1*^{OX} tumors (Fig. 3 C). To this end, we performed pseudo-time analysis to infer the activation status (Monocle pseudo-time) for individual CD8$^+$ T cells according to their transcriptome profiles. By examining cell distribution along the activation (pseudo-time) trajectory, we found that CD8$^+$ T cells in *Mcrs1*^{OX} tumors tended to aggregate towards the end of the trajectory, where genes involved in late CD8$^+$ T cell activation were highly expressed, such as *Cd44*, *Nr4a2*, *Havcr2*, *Pdcd1*, *Lag3*, and *Prf1* (Fig. 3 C). To further differentiate the functional states of CD8$^+$ T cells, we performed a dimension reduction analysis of the pseudo-time estimates of CD8$^+$ T cells (Fig. 3 D). This resulted in a bifurcated trajectory with three branches corresponding to activating/proliferating, effector (post-activation), and memory cells, respectively. We found that CD8$^+$ T cells in *Mcrs1*^{OX} tumors preferentially accumulated at the effector branch (Fig. 3 D). This was independently confirmed by flow cytometry analysis, with a significant increase of CD8$^+$ effector T cells (IFN-γ$^+$ or KLRG1$^+$ CD127$^{-/low}$) in *Mcrs1*^{OX} tumors compared to control tumors (Fig. 3, E and F). A similar increase of IFN-γ$^+$ CD4$^+$ T was also observed in *Mcrs1*^{OX} tumors (Fig. S3 D). Therefore, elevated *Mcrs1* expression in pancreatic cancer drove T cells further down the activation trajectory into the effector state.

CD8$^+$ T cells recognizing tumor antigens undergo clonal expansion during a productive anti-tumor response. We thus profiled the clonotypes of CD8$^+$ T cells with scTCR-seq (Fig. 3 G). While the majority of the TCRs were only detected in one cell, there were 8.3%, and 26.0% of TCR clonotypes could be detected in at least two cells in control and *Mcrs1*^{OX} tumors, respectively, indicating the activation and extensive clonal expansion of CD8$^+$ T cells in *Mcrs1*^{OX} tumors. As clonal expansion reduced the evenness of TCR distribution, we quantified TCR clonotype evenness with the Gini Index. We found that the TCR Gini Index of *Mcrs1*^{OX} tumors (0.35) was markedly higher than that of control tumors (0.12), indicative of more robust clonal expansion in *Mcrs1*^{OX} tumors. Next, we focused on clonotypes expanded in tumors, which potentially represented tumor-targeting T cells (Fig. 3 H). Compared to control tumors, expanded clones in *Mcrs1*^{OX} tumors were distributed along the functional continuum of CD8$^+$ T cells, aggregating toward the end of the effector

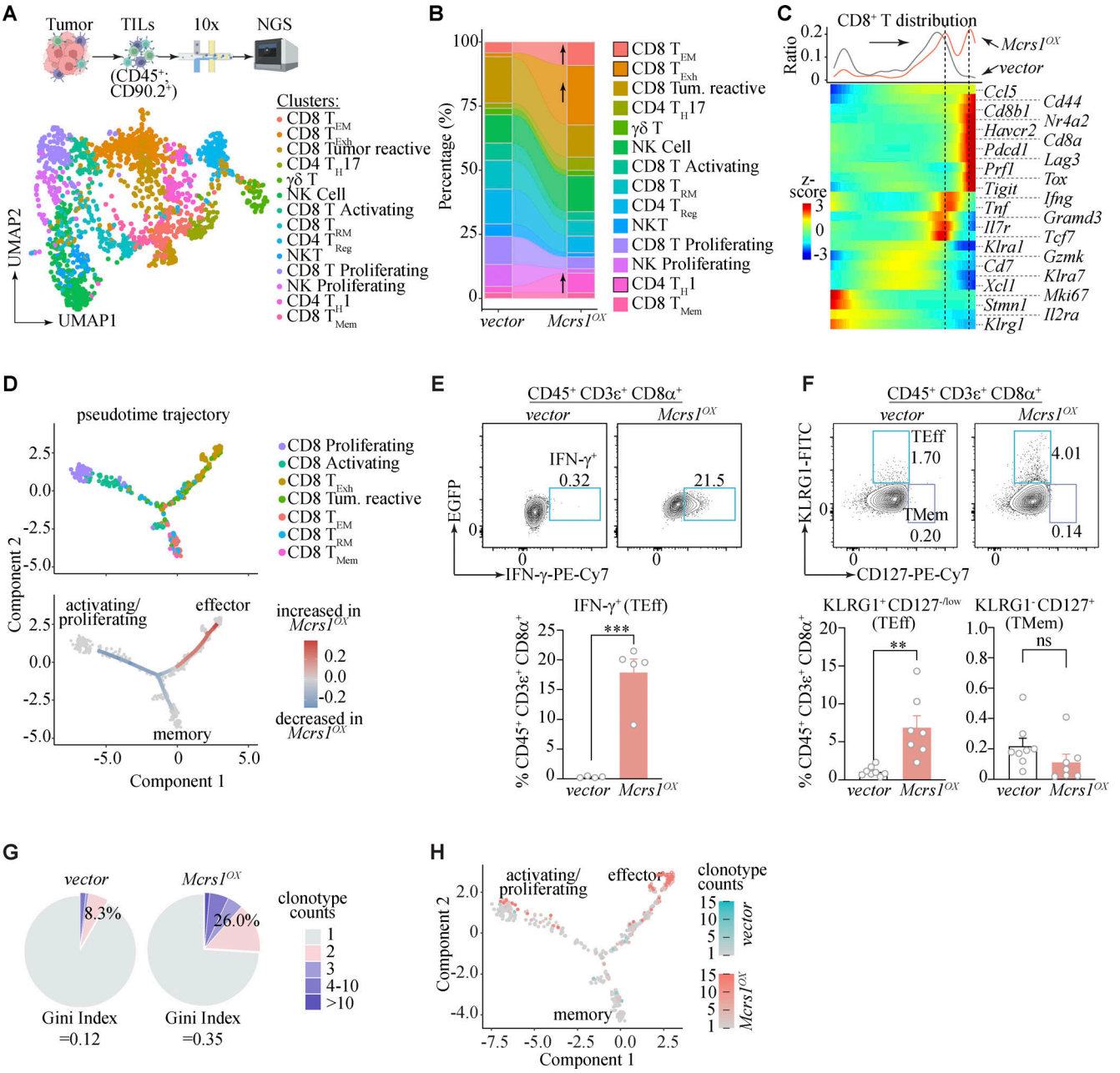

Figure 3. **Elevated *Mcrs1* expression activates T cell–mediated anti-tumor immunity in vivo. (A)** TILs ($CD45^+$ $CD90.2^+$) were isolated from subcutaneous $Mcrs1^{OX}$ and vector control tumors, multiplexed with hashtags, and subjected to scRNA-seq and scTCR-seq analysis. The UMAP embedding of various cell clusters is shown (samples were pooled from $n = 3$ mice for each group). NGS, next-generation sequencing. Illustration was created with https://BioRender.com with modifications. **(B)** Comparison of cell percentages of different cell clusters between $Mcrs1^{OX}$ or vector control tumors. Upward arrows indicate increases in the cell clusters. T_{RM}, tissue-resident memory T cell; T_{Reg}, regulatory T cell; T_{Mem}, memory T cell. **(C)** Distribution of $CD8^+$ T cells along the pseudotime trajectory. **(D)** Scatter plots showing the projected pseudo time (states) of $CD8^+$ T cells in individual clusters (upper panel). The enrichment of effector $CD8^+$ T cells in $Mcrs1^{OX}$ tumors is shown in the lower panel. **(E)** Frequencies of $CD8^+$ effector T cells (T_{Eff}) in $Mcrs1^{OX}$ and vector control tumors assessed by IFN-γ expression, with representative flow plots (upper panel) and quantification (lower panel) shown ($n = 4, 5$ for vector control and $Mcrs1^{OX}$, respectively; presented as means ± SEM; ***, $P < 0.001$; two-tailed unpaired *t* test; $N > 3$ independent experiments). **(F)** Frequencies of $CD8^+$ T_{Eff} in $Mcrs1^{OX}$ and vector control tumors assessed by KLRG1 and CD127 expression, with representative flow plots (upper panel) and quantification (lower panel) shown ($n = 8, 7$ for vector control and $Mcrs1^{OX}$, respectively; presented as means ± SEM; ns, not significant, $P \geq 0.05$; **, $P < 0.01$; two-tailed unpaired *t* test; $N > 3$ independent experiments). **(G)** Fractions of $CD8^+$ T cells showing clonal expansion (detected in >1 cell) in $Mcrs1^{OX}$ and vector control tumors revealed by scTCR-seq. The Gini Index of TCR clonotypes is calculated to reflect the extent of clonal expansion (unevenness of clonotype distribution). **(H)** Distribution of clonally expanded $CD8^+$ T cells along the projected pseudo-time, showing $CD8^+$ T cells expanding into the effector state in $Mcrs1^{OX}$ tumors.

branch, indicative of enhanced activation of tumor-targeting T cells. Together, our data showed that elevated *Mcrs1* expression in pancreatic cancer cells elicited active CD8⁺ T cell responses, underlying its immune-sensitizing effects.

Mcrs1 enhances MHC-I–mediated antigen presentation by binding to MHC-I loci

We next sought to investigate the mechanism by which MCRS1 activated CD8⁺ T cell responses. Given the complex interaction between tumor and immune cells in vivo, we examined the tumor-intrinsic effects by analyzing the transcriptomes of the vector control and *Mcrs1*^{OX} cells cultured in vitro. We specifically focused on genes that were regulated by MCRS1 both in vivo and in vitro by integrating RNA-seq data from tumors and cultured cells (Fig. 4 A). Gene set enrichment analysis (GSEA) revealed that IFN-α/β/γ signaling and MHC-I antigen presentation pathways were among the top enriched pathways in *Mcrs1*^{OX} cells compared to vector control cells (Fig. 4 B), which are well known to promote CD8⁺ T cell–mediated anti-tumor immunity by remodeling the tumor microenvironment and increasing tumor recognition, respectively (Parker et al., 2016; Pishesha et al., 2022).

To assess the contribution of IFN signaling in MCRS1-induced immune sensitization, we compared the expression of IFN molecules in vector control and *Mcrs1*^{OX} cells. We found that *Mcrs1*^{OX} cells expressed higher *Ifna1* (encoding IFN-α1) and lower *Ifnb1* (encoding IFN-β1) than control cells (Fig. S4 A), while no difference was detected for type 2 (*Ifng*) and type 3 (*Ifnl2* and *Ifnl3*) interferons. Critically, when inoculated into *Ifnar1*$^{-/-}$ mice that were deficient in IFN-α/β signaling, *Mcrs1*^{OX} tumors still displayed reduced growth than control tumors (Fig. 4, C and D). Thus, IFN signaling was unlikely to be a significant pathway underlying the immune-sensitizing effect of MCRS1.

MHC-I antigen presentation is a prerequisite to the antigen recognition and effector functions of CD8⁺ T cells. Low MHC-I antigen presentation is a critical immune evasion mechanism of pancreatic cancer (Ho et al., 2020; Pommier et al., 2018; Yamamoto et al., 2020b). Thus, upregulation of the MHC-I antigen presentation pathway could increase the immunogenicity of tumor cells and lead to enhanced immune recognition and killing, which we hypothesized might underlie the immune-sensitizing effect of MCRS1. To test this hypothesis, we examined the surface display of MHC-I molecules by flow cytometry as MHC-I molecules are retained in the ER until antigenic peptides are properly loaded for presentation (Pishesha et al., 2022). In line with our transcriptome data, we found that *Mcrs1*^{OX} cells displayed higher frequencies and intensities of MHC-I at the cell surface than control cells (Fig. 4, E and F), indicating enhanced antigen presentation. This result was also consistent with the enhanced killing of *Mcrs1*^{OX} cells by CD8⁺ T cells in vitro (Fig. 2, A and B) and the induction of active CD8⁺ T cell responses in vivo (Fig. 3). Conversely, knocking out *Mcrs1* in HT cells resulted in reduced expression of MHC-I genes, *H2-K1*, *H2-D1*, and *H2-Q4* (Fig. 4 G and Fig. S4 B).

We next sought to investigate the mechanism by which MCRS1 regulated MHC-I genes in pancreatic cancer cells. We observed no upregulation of *Nlrc5* (Fig. S4 C), a critical transcriptional regulator of MHC-I genes (Kobayashi and van den Elsen, 2012), indicating that MCRS1 was unlikely to regulate MHC-I through *Nlrc5*. Because IFN-α signaling is known to induce MHC-I genes (Parker et al., 2016) and was upregulated in *Mcrs1*^{OX} cells (Fig. S4 A), we blocked IFN-α signaling with an antibody targeting IFNAR1 or an inhibitor against JAK kinases (Fig. 4 H and Fig. S4 D). While largely reversing the expression of IFN-stimulated genes (ISGs) (*Isg15* and *Oas2*), blocking IFNAR1 and inhibiting JAKs marginally reduced the expression of MHC-I genes, *H2-K1* and *H2-D1*, in *Mcrs1*^{OX} cells. Together, our data suggested that IFN-α signaling marginally accounted for MHC-I upregulation by MCRS1, arguing for alternative pathways employed by MCRS1 to regulate MHC-I.

Because MCRS1 is a transcriptional regulator, we wanted to test whether MCRS1 could regulate MHC-I directly. To this end, we performed chromatin immunoprecipitation coupled with deep sequencing (ChIP-seq) to unbiasedly profile the direct targets of MCRS1 (Fig. 4 I). MCRS1 binding peaks were broadly distributed across the genome (Fig. 4 I and Fig. S4 E), with a significant fraction of peaks located in the proximity of the transcription start site (TSS). We identified 5210 MCRS1-bound genes that were expressed in the HT pancreatic cancer cells (Fig. S4 F), which displayed stronger MCRS1 binding than non-expressed genes. Indeed, these MCRS1-bound genes exhibited greater expression changes in *Mcrs1*^{OX} cells than unbound genes (Fig. S4, G and H), suggesting that MCRS1 could bind to the gene promoters and regulate gene expression.

To examine whether MCRS1 could directly regulate MHC-I genes, we performed pathway analysis of MCRS1 target genes, which revealed the enrichment of genes involved in MHC-I–mediated antigen presentation (Fig. 4 J and Fig. S4 I). Indeed, substantial MCRS1 binding could be detected in the promoter regions of *H2-K1*, *H2-D1*, and *H2-Q4*, consistent with their increased expression in *Mcrs1*^{OX} cells (Fig. 4 K). Strikingly, analysis of a published MCRS1 ChIP-seq dataset revealed that MCRS1 could also bind to MHC-I genes (*HLA-A/B/C*) in a human hepatocellular carcinoma cell line (HepG2) (Runge et al., 2018) (Fig. S4 J), suggesting that regulation of MHC-I by MCRS1 might be conserved in mice and humans. Together, our data indicated that MCRS1 could directly bind to and regulate the expression of MHC-I genes.

To directly examine the regulation of antigen presentation activity by MCRS1, we transduced control and *Mcrs1*^{OX} cells with the chicken *Ovalbumin* ORF (*OVAL*), the model antigen that could be processed into the SIINFEKL octapeptide (OVA) and presented by MHC-I (Rotzschke et al., 1991) (Fig. 4 L). Despite comparable *OVAL* expression in control and *Mcrs1*^{OX} cells, we observed a significant increase in the surface display of the MHC-I:OVA complex by *Mcrs1*^{OX} cells than control cells, indicative of enhanced antigen processing and presentation activities in *Mcrs1*^{OX} cells. Next, we examined the T cell activation capacities of *OVAL*-expressing cancer cells by co-culturing with CD8⁺ OT-I T cells (Fig. 4 M), a setting mirroring tumor recognition by primed effector T cells at the tumor site. In line with enhanced MHC-I antigen presentation, we found that *Mcrs1*^{OX} cells stimulated more extensive proliferation of OT-I T cells than control cells (Fig. 4 M), indicative of increased tumor

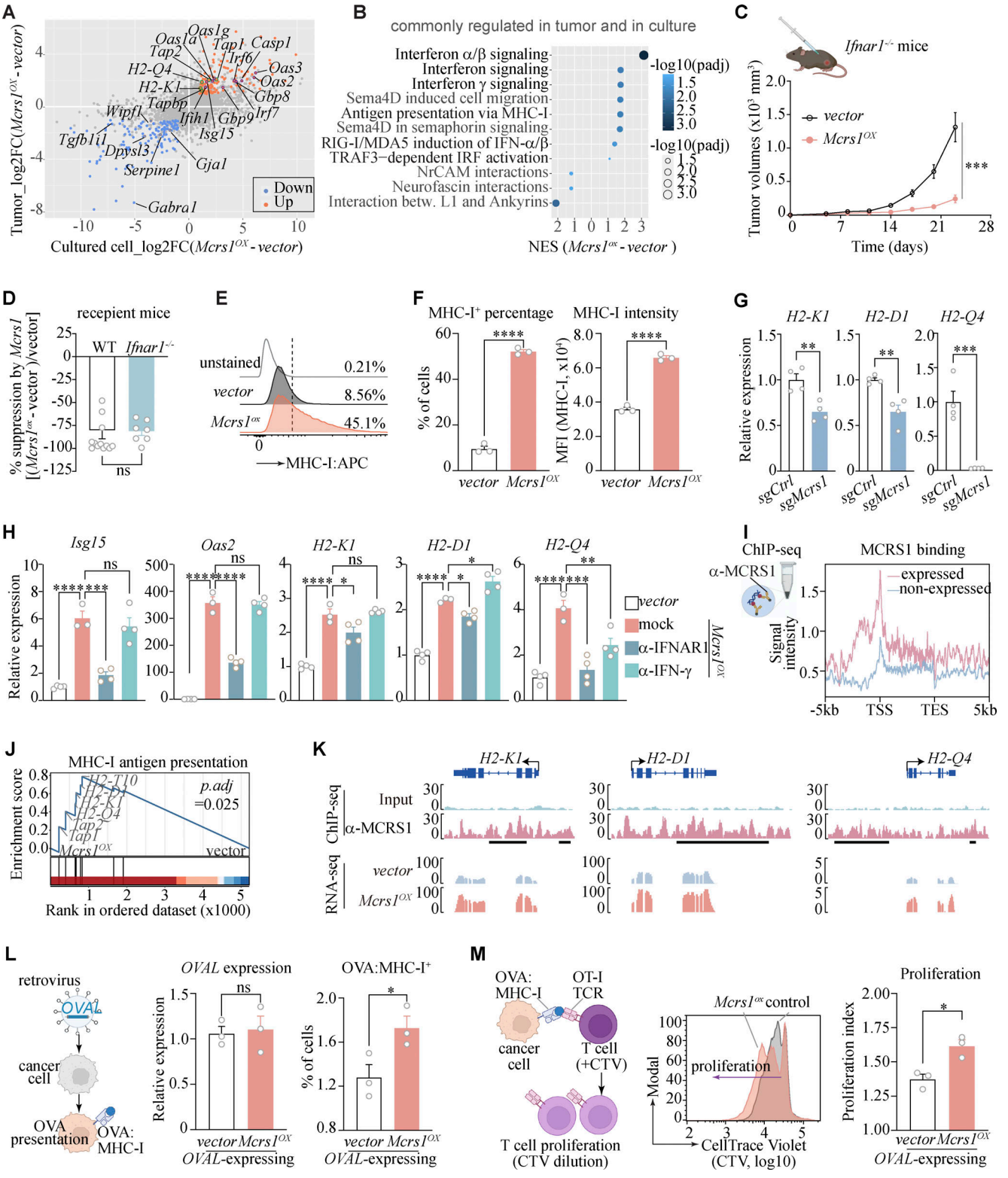

Figure 4. ***Mcrs1* enhances MHC-I–mediated antigen presentation by binding to MHC-I loci. (A)** RNA-seq analysis of differentially expressed genes between *Mcrs1*^{OX} and vector control cells in vitro (x-axis, cell culture, *n* = 3 for each group) and in vivo (y-axis, tumor, *n* = 4 for each group). **(B)** GSEA analysis of pathways commonly regulated by *Mcrs1* in vitro and in vivo. IRF, interferon regulatory factors; L1, L1-type cell adhesion molecules. **(C)** The growth curve of *Mcrs1*^{OX} and vector control tumors in *Ifnar1*$^{-/-}$ mice (*n* = 7 for both groups; presented as means ± SEM; ***, P < 0.001; two-way ANOVA; *N* = 2 independent experiments). Illustration was created with https://BioRender.com. **(D)** Tumor suppression by *Mcrs1* in WT (SLAC) and *Ifnar1*$^{-/-}$ mice, calculated as the volume reduction of *Mcrs1*^{OX} tumors compared to vector control tumors as a fraction of control tumor volumes (*n* = 12, 7 for WT and *Ifnar1*$^{-/-}$, respectively; presented as means ± SEM; ns, not significant, P ≥ 0.05; two-tailed unpaired *t* test; *N* = 2 independent experiments). **(E)** Representative histograms showing surface staining of MHC-I in *Mcrs1*^{OX} and vector control cells (*N* > 3 independent experiments). **(F)** Summary of the MHC-I^{+} frequency and mean fluorescence intensity

(MFI) of MHC-I in *Mcrs1*^{OX} and vector control cells (n = 3 for both groups; presented as means ± SEM; ****, P < 0.0001; two-tailed unpaired t test; N > 3 independent experiments). **(G)** Expression of MHC-I genes (*H2-K1*, *H2-D1*, *H2-Q4*) in *Mcrs1* knockout cells (*sgMcrs1*) (n = 4 for both groups; presented as means ± SEM; **, P < 0.01; ***, P < 0.001; two-tailed unpaired t test; N > 3 independent experiments). **(H)** Expression of MHC-I genes (*H2-K1*, *H2-D1*, *H2-Q4*) in *Mcrs1*^{OX} cells when IFN-α/β and IFN-γ signaling were blocked by blocking antibodies against IFNAR1 and IFN-γ. Known ISGs, *Isg15* and *Oas2*, were used as controls (n = 4, 3, 4, 4 for control, *Mcrs1*^{OX}, α-IFNAR1, and α-IFN-γ, respectively; presented as means ± SEM; ns, not significant, P ≥ 0.05; *, P < 0.05; **, P < 0.01; ***, P < 0.001; ****, P < 0.0001; one-way ANOVA with Tukey's multiple comparisons test; N = 2 independent experiments). **(I)** MCRS1 binding sites in the genome were profiled by ChIP-seq. MCRS1 binding intensities in expressed and non-expressed genes are plotted according to the distances to the transcription start sites (TSS) and transcription end site (TES) (n = 2 for both groups; N = 2 independent experiments). Illustration was created with https://BioRender.com. **(J)** Enrichment of MHC-I antigen presentation pathways in MCRS1-target genes revealed by GSEA analysis. **(K)** Representative genomic alignment of MCRS1 ChIP-seq and RNA-seq at the *H2-K1*, *H2-D1*, and *H2-Q4* loci. **(L)** Presentation of the model antigen OVA by *Mcrs1*^{OX} and vector control cells. Cells were transduced with OVA-encoding (*OVAL*) retrovirus, and the mRNA expression of *OVAL* and surface presentation of processed OVA antigen complexed with MHC-I were examined by qPCR and flow cytometry with the 25-D1.16 monoclonal antibody, respectively (n = 3 for all groups; presented as means ± SEM; ns, not significant, P ≥ 0.05; *, P < 0.05; two-tailed unpaired t test; N = 2 independent experiments). Illustration was created with https://BioRender.com with modifications. **(M)** T cell activation by presented OVA antigen in *Mcrs1*^{OX} and vector control cells. OVA-expressing *Mcrs1*^{OX} and vector control cells were incubated with CellTrace Violet (CTV) dye-loaded OT-I T cells. Antigen (OVA)-stimulated activation and proliferation of OT-I T cells were monitored by CTV dilution. Representative histograms of CTV dilution (left panel) and the calculated proliferation index are shown (n = 3 for all groups; presented as means ± SEM; *, P <0.05; two-tailed unpaired t test; N > 3 independent experiments). Illustration was created with https://BioRender.com with modifications.

recognition and effector T cell activation. Together, our data demonstrated that MCRS1 enhanced MHC-I–mediated antigen presentation, thereby increasing the immunogenicity of pancreatic cancer and stimulating CD8$^+$ T cell responses.

MCRS1 upregulates MHC-I by interacting with YY1

Next, we sought to determine the molecular mechanism by which MCRS1 upregulated MHC-I expression. MCRS1 lacks the DNA-binding domain and is involved in regulatory complexes such as the SWI/SNF complex (SWItch/Sucrose Non-Fermentable), the INO80 complex (INOsitol-requiring mutant 80), and the NSL complex (NonSpecific-Lethal) in various cell and tissue types (Huang et al., 2022). To identify potential MCRS1-interacting partners underlying the immune sensitizing effect in pancreatic cancer, we performed immunoprecipitation against the FLAG-tagged MCRS1, followed by mass spectrometry (Fig. 5 A). The top enriched protein was MCRS1 itself, followed by subunits of multiple regulatory complexes that were known to involve MCRS1, such as KANSL2, YY1, WDR5, and KAT8. STRING analysis of enriched proteins revealed an MCRS1-centered protein–protein interaction network, with numerous nodes corresponding to subunits of the INO80 complex or the NSL complex (Fig. 5 B). This raised the possibility that MCRS1 might regulate MHC-I expression through chromatin remodeling.

To test this hypothesis, we knocked out *Yy1* and *Kat8* in *Mcrs1*^{OX} cells, critical subunits of the INO80 and NSL complexes, respectively (Fig. 5 C and Fig. S5 A). While knocking out *Kat8* showed little to no effects, knocking out *Yy1* largely reverted the upregulation of MHC-I genes (*H2-K1*, *H2-D1*, and *H2-Q4*) in *Mcrs1*^{OX} cells, suggesting that MCRS1 could regulate MHC-I expression via YY1. Supporting our hypothesis, we found increased MCRS1–YY1 interaction in *Mcrs1*^{OX} cells (Fig. 5 D), corroborated by the enrichment of the YY1-binding motif in MCRS1-bound genomic regions (Fig. 5 E). This suggested that MCRS1 and YY1 co-regulated downstream gene expression. Indeed, elevating *Yy1* expression increased the expression of MHC-I genes in HT cells (Fig. 5 F and Fig. S5 B), phenocopying that of *Mcrs1*. Furthermore, we found that MCRS1 and YY1 were co-expressed by tumor cells in human PDAC samples (Fig. S5 C) and co-occupied the human MHC-I loci (*HLA-A/B/C*) in HepG2 cells (Runge et al., 2018) (Fig. S5 D). Therefore, these data suggested that MCRS1 could regulate MHC-I gene expression by interacting with YY1. This was also consistent with previous reports that YY1 suppresses pancreatic cancer progression in mice and humans (Zhang et al., 2014, 2017) and that YY1 regulates human *HLA-A* and mouse *H2-Eα* in melanoma and B cell lymphoma cells, respectively (Griffioen et al., 2000; Liao et al., 2004).

MCRS1 and YY1 coordinately regulate chromatin accessibility and immune sensitivity

We next sought to investigate how MCRS1 and YY1 regulated MHC-I expression. As YY1 has recently been recognized to regulate the 3D chromatin structure, which is critical for gene expression (Weintraub et al., 2017), we reasoned that MCRS1 could participate in this process. To this end, we examined the effects of MCRS1 and YY1 on chromatin accessibility in control (*vector*;*sgCtrl*), *Mcrs1*^{OX};*sgCtrl*, and *Mcrs1*^{OX};*sgYy1* cells by assay for targeting accessible-chromatin with high-throughout sequencing (ATAC-seq). The chromatin accessibility was slightly increased around TSS in *Mcrs1*^{OX} cells compared to control cells (Fig. 6 A), which could be reversed by *Yy1* knockout, suggesting that MCRS1 overly increased chromatin accessibility in a YY1-dependent manner. Notably, there was a significant positive correlation between changes in chromatin accessibility and changes in gene expression in control and *Mcrs1*^{OX} cells (Fig. S5 E), suggesting that MCRS1 and YY1 could coordinately regulate gene expression via chromatin remodeling.

To examine the role of MCRS1/YY1-mediated chromatin remodeling in pancreatic cancer progression, we aligned the chromatin accessibility profiles of control, *Mcrs1*^{OX};*sgCtrl*, and *Mcrs1*^{OX};*sgYy1* cells to those of mouse primary pancreatic tumors at different tumorigenesis stages (Burdziak et al., 2023) (Fig. S5 F). We found that elevated *Mcrs1* expression reversed the tumorigenesis trajectory of pancreatic cancer cells, which could be partially abolished by *Yy1* knockout, indicating that MCRS1/YY1-mediated chromatin remodeling suppressed the progression of pancreatic tumors.

By unsupervised clustering, we found that genes that were bound and regulated by MCRS1 could be clustered into five

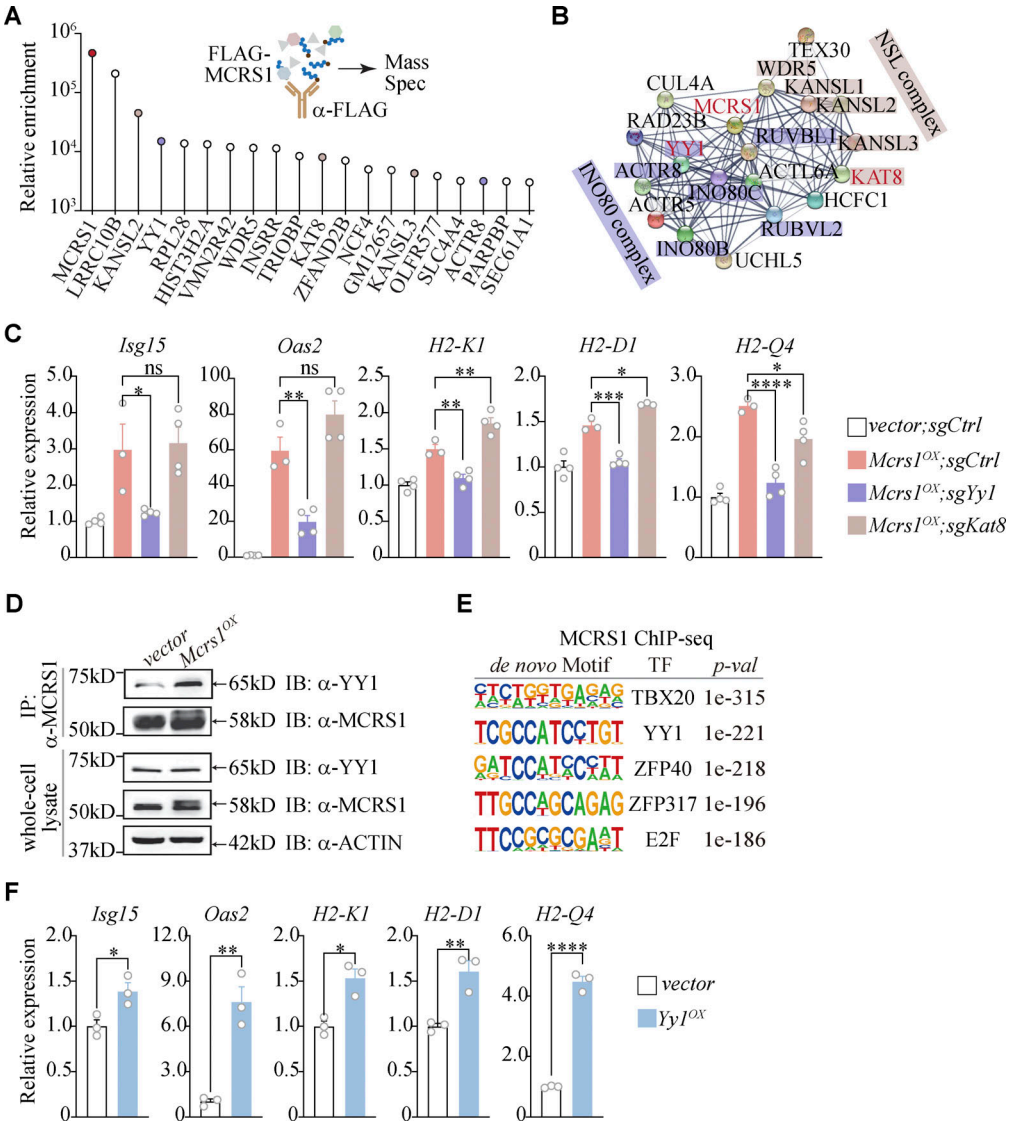

Figure 5. **MCRS1 upregulates MHC-I by interacting with YY1. (A)** Identification of MCRS1-interacting proteins in mouse pancreatic cancer cells by IP-MS, with top hits shown (n = 1 for both groups). **(B)** STRING analysis of MCRS1-interacting proteins, with interaction detected between MCRS1 and YY1 and KAT8. **(C)** Expression of ISGs and MHC-I genes in *Mcrs1*^{OX} cells that were deficient in *Yy1* or *Kat8* by CRISPR-mediated gene knockout (n = 4, 3, 4, 4 for control, *Mcrs1*^{OX}, *Mcrs1*^{OX}*;sgYy1*, and *Mcrs1*^{OX}*;sgKat8*, respectively; presented as means ± SEM; ns, not significant, P ≥ 0.05; *, P < 0.05; **, P < 0.01; ***, P < 0.001; ****, P < 0.0001; one-way ANOVA with Tukey's multiple comparisons test; N = 2 independent experiments). **(D)** Increased MCRS1–YY1 interaction in *Mcrs1*^{OX} cells assessed by immunoprecipitation (N > 3 independent experiments). **(E)** De novo motif discovery of MCRS1-bound genomic regions, with the YY1 binding motif among the top enriched motifs. **(F)** Expression of ISGs and MHC-I genes in *Yy1*^{OX} cells (n = 3 for both groups; presented as means ± SEM; *, P < 0.05; **, P < 0.01; ****, P < 0.0001; two-tailed unpaired t test; N = 2 independent experiments). Source data are available for this figure: SourceData F5.

groups according to their chromatin accessibility in control, *Mcrs1*^{OX}*;sgCtrl*, and *Mcrs1*^{OX}*;sgYy1* cells (Fig. 6 B). Interestingly, the chromatin accessibilities of Cluster 1 genes were increased in *Mcrs1*^{OX} cells and decreased in *Mcrs1*^{OX}*;sgYy1* cells, while the chromatin accessibilities of Cluster 2 genes showed the opposite pattern. We thus reasoned that the chromatin of Cluster 1 and 2 genes could be subjected to MCRS1/YY1-dependent remodeling. In particular, key genes of the MHC-I pathway, including *H2-K1*, *H2-D1*, and *H2-Q4*, fell into Cluster 1 (Fig. 6 B), with increased chromatin accessibility in *Mcrs1*^{OX} cells that was largely restored in *Mcrs1*^{OX}*;sgYy1* cells. Importantly, changes in chromatin accessibility in distal non-coding regions of these gene loci appeared consistent with gene expression changes in control, *Mcrs1*^{OX}*;sgCtrl*, and *Mcrs1*^{OX}*;sgYy1* cells (Fig. 6 C), indicating that MCRS1 and YY1 might coordinately regulate MHC-I expression through these distal non-coding elements. Through integrative multi-omics analysis, we found that the MHC-I genes were among the 39 overlapping genes that were bound by MCRS1, differentially expressed in *Mcrs1*^{OX} cells and tumors, and subjected to MCRS1/YY1-dependent chromatin remodeling (Fig. 6 D and Table S2). Therefore, our data suggested that MCRS1 and YY1 regulated MHC-I gene expression by modulating chromatin accessibility.

Lastly, we sought to determine whether the immune-sensitizing effect of MCRS1 was dependent upon YY1 in vivo.

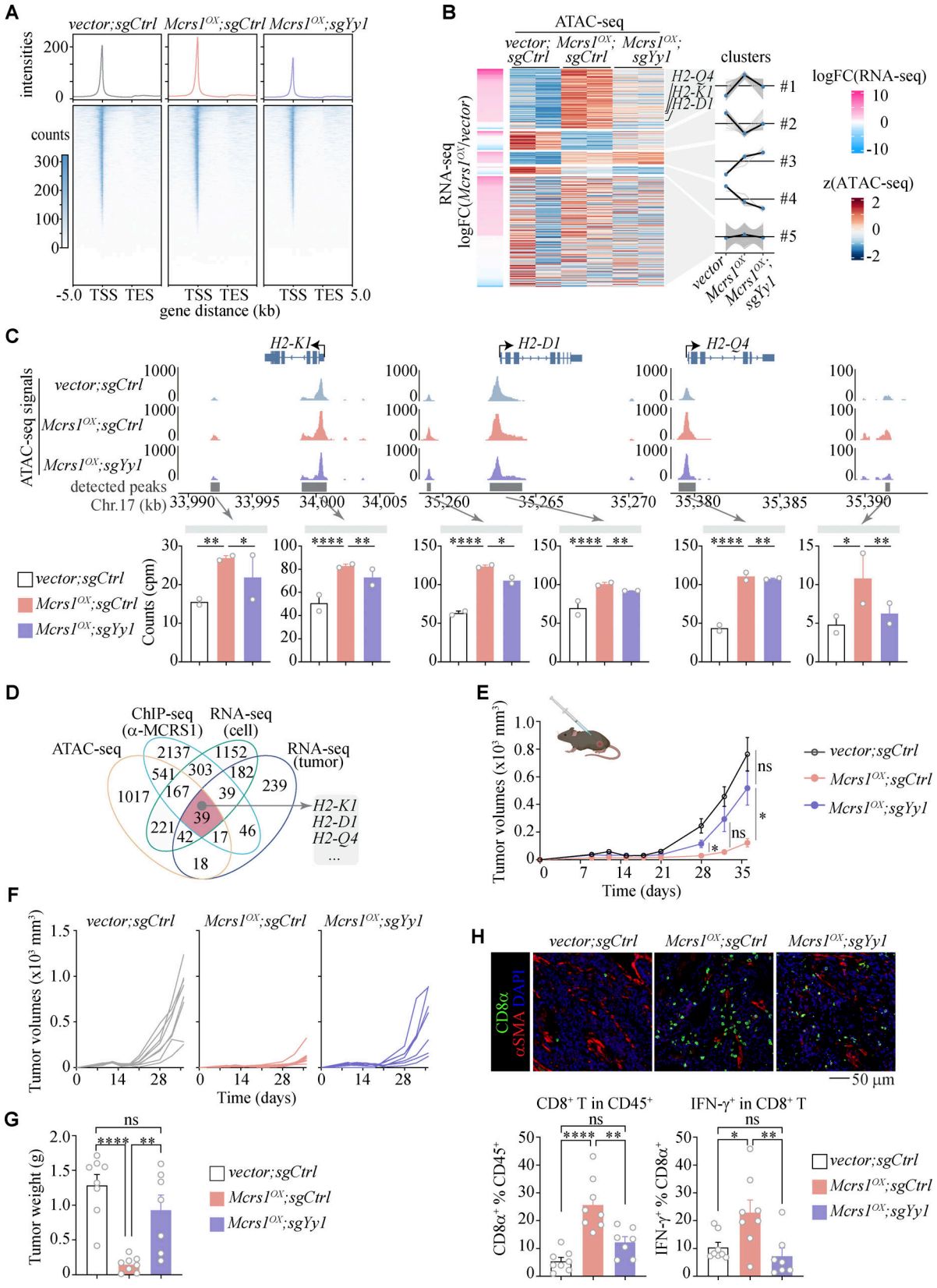

Figure 6. **MCRS1 and YY1 coordinately regulate chromatin accessibility and immune sensitivity. (A)** Metaplot and heatmap showing ATAC-seq signals around the TSS in control, *Mcrs1*^{OX}, and *Mcrs1*^{OX};*sgYy1* cells (n = 2 for both groups). **(B)** ATAC-seq profiles of genes that were bound by MCRS1 and differentially expressed in *Mcrs1*^{OX} cells. Genes were clustered based on ATAC-seq profiles, with the mean ATAC signals for each cluster shown on the right. **(C)** Chromatin accessibility at the MHC-I loci determined by ATAC-seq, with the upper panel showing tracks of ATAC-seq signals and the lower panel showing quantification of peaks around the TSS or distal non-coding regions (n = 2 for both groups; presented as means ± SEM; *, P < 0.05; **, P < 0.01; ****, P < 0.0001; MAnorm test).

(D) MCRS1-regulated genes identified by differential expression in *Mcrs1*^{OX} cell and tumor (RNA-seq), direct binding by MCRS1 (ChIP-seq), and MCRS1/YY1-dependent chromatin accessibility change (ATAC-seq). A total of 39 genes met all these criteria, including the MHC-I genes. **(E)** The growth curves of control, *Mcrs1*^{OX}, and *Mcrs1*^{OX}*;sgYy1* tumors in WT mice (n = 8, 8, 7 for control, *Mcrs1*^{OX}, and *Mcrs1*^{OX}*;sgYy1*, respectively; presented as Means ± SEM; ns, not significant, P ≥ 0.05; *, P < 0.05; two-way ANOVA with Tukey's multiple comparisons test; N = 3 independent experiments). Illustration was created with https://BioRender.com. **(F)** Spider plots showing tumor volume changes in individual mice tumors as in E. **(G)** Tumor weights at the point of sacrifice (n = 8, 8, 7 for control, *Mcrs1*^{OX}, and *Mcrs1*^{OX}*;sgYy1*, respectively; presented as means ± SEM; ns, not significant, P ≥ 0.05; **, P < 0.01; ****, P < 0.0001; one-way ANOVA with Tukey's multiple comparisons test; N = 3 independent experiments). **(H)** Analysis of CD8$^+$ T cells in control, *Mcrs1*^{OX}, and *Mcrs1*^{OX}*;sgYy1* tumors, analyzed by immunofluorescent staining (upper panel) and flow cytometry (lower panel) (n = 8, 8, 7 for control, *Mcrs1*^{OX}, and *Mcrs1*^{OX}*;sgYy1*, respectively; presented as means ± SEM; ns, not significant, P ≥ 0.05; *, P < 0.05; **, P < 0.01; ****, P < 0.0001; one-way ANOVA with Tukey's multiple comparisons test; N = 3 independent experiments). Scale bar = 50 µm.

To this end, we inoculated control, *Mcrs1*^{OX}*;sgCtrl*, and *Mcrs1*^{OX}*;sgYy1* cells into mice and found that *Mcrs1*^{OX}*;sgYy1* tumors showed significantly increased growth compared to *Mcrs1*^{OX}*;sgCtrl* tumors, similar to control tumors (Fig. 6, E–G), suggesting that YY1 was required for MCRS1-mediated immune sensitization. Furthermore, activated CD8$^+$ effector T cells were also decreased in *Mcrs1*^{OX}*;sgYy1* tumors compared to *Mcrs1*^{OX}*;sgCtrl* tumors (Fig. 6 H), consistent with reduced MHC-I gene expression in YY1-deficient cells (Fig. 5 C). A similar decrease in CD4$^+$ effector T cells could also be detected in *Mcrs1*^{OX}*;sgYy1* tumors (Fig. S5 G). Taken together, our study showed that MCRS1 and YY1 coordinately regulate MHC-I expression in pancreatic cancer cells and thereby sensitized cancer cells to T cell–mediated anti-tumor immunity.

MCRS1 sensitizes α-PD-1 immunotherapy in mice and humans

Given its potent immune-sensitizing effect, we wanted to test whether MCRS1 could improve immunotherapy against pancreatic cancer in mice. To this end, we treated vector control and *Mcrs1*^{OX} tumors with a blocking antibody against the immune checkpoint PD-1 (α-PD-1) (Fig. 7 A). Mirroring the clinical challenge of immunotherapy against pancreatic cancer, α-PD-1 treatment had no detectable effect on the growth of the control tumors. On the contrary, α-PD-1 treatment further reduced the growth of *Mcrs1*^{OX} tumors (Fig. 7, A and B) and resulted in smaller tumor weights at the time of sacrifice (Fig. 7 C). These data suggested that MCRS1 could sensitize pancreatic tumor cells to α-PD-1 immunotherapy.

Given the ineffectiveness of immunotherapy against human PDAC, the scarcity of clinical data limited the direct evaluation of MCRS1's impact on α-PD-1 treatment in PDAC patients. Because chemotherapy has been shown to act partly by stimulating anti-tumor immunity via cell damage (Gotwals et al., 2017; Metcalf et al., 2021), we reasoned that immune sensitization by MCRS1 could amplify such effects to enhance treatment efficacy further. To this end, we retrospectively assessed the relationship between MCRS1 expression and tumor responses to neoadjuvant chemotherapy (NAC) in PDAC patients (Table S3). We found that high MCRS1 levels were associated with lower tumor regression grade (TRG) scores after treatment (Fig. 7 D), indicative of greater treatment responses and tumor regression. Remarkably, patients with high MCRS1 expression showed significantly extended overall and progression-free survival time compared to those with low MCRS1 expression (Fig. 7, E and F). Together, our data suggested that MCRS1 levels could serve as an independent predictor for favorable chemotherapy outcomes in PDAC patients, in line with its immune-sensitizing effect.

Reduced MHC-I antigen presentation represents a common obstacle for immunotherapy in many types of cancers beyond PDAC (Maleki Vareki, 2018). Given that MCRS1 expression was positively correlated with T cell activation in the majority of TCGA tumor types (Fig. 1 D) and that MCRS1 bound to human MHC-I genes in HepG2 cells (Fig. S4 J), we hypothesized that MCRS1 might regulate MHC-I expression in other tumor types. Indeed, by examining the correlation between *MCRS1* and *MHC-I* expression in the TCGA database, we found that *MCRS1* expression was positively correlated with the expression of human MHC-I (*HLA-A,B,C*) in a wide range of cancer types (Fig. 7 G), including PAAD and lung adenocarcinoma, which was consistent with our observation that *MCRS1* expression was positively correlated with T cell activities in the majority of TCGA cancer types (Fig. 1 D).

Therefore, we reasoned that MCRS1 might sensitize other cancers to α-PD-1 immunotherapy. To this end, we examined the impact of MCRS1 on immunotherapy in advanced non-small cell lung cancer (NSCLC), for which ICB therapy represents a critical modality for patients ineligible for surgical intervention. By retrospectively examining MCRS1 expression in puncture samples of 107 patients subjected to α-PD-1 treatment (Fig. 7 H and Table S4), we found that elevated MCRS1 expression correlated with increased responsiveness to α-PD-1 therapy, evidenced by extended overall and progression-free survival periods (Fig. 7, I and J). Intriguingly, by paired analysis of the NSCLC biopsies before and after α-PD-1 treatment, we found that MCRS1 expression was decreased after α-PD-1 treatment (Fig. 7, K and L), particularly in patients with high MCRS1 expression prior to treatment. This suggested that T cells reinvigorated by α-PD-1 treatment preferentially eliminated NSCLC cells with high MCRS1 expression, in line with the increased α-PD-1 efficacy in patients with high MCRS1 expression. In aggregate, our data suggested that elevated MCRS1 sensitized cancer cells to α-PD-1 therapy in mice and humans.

Discussion

T cell–mediated anti-tumor immunity is central to the emerging immunotherapy against cancer and also contributes to the efficacy of conventional chemo- and radiotherapies (Gotwals et al., 2017; Waldman et al., 2020). ICB therapy, which has markedly advanced the treatment landscape for various solid neoplasms and brought substantial clinical gains, functions through unleashing the activity of pre-existing T cell immunity. Because T cells critically depend on antigens presented by MHC-I to

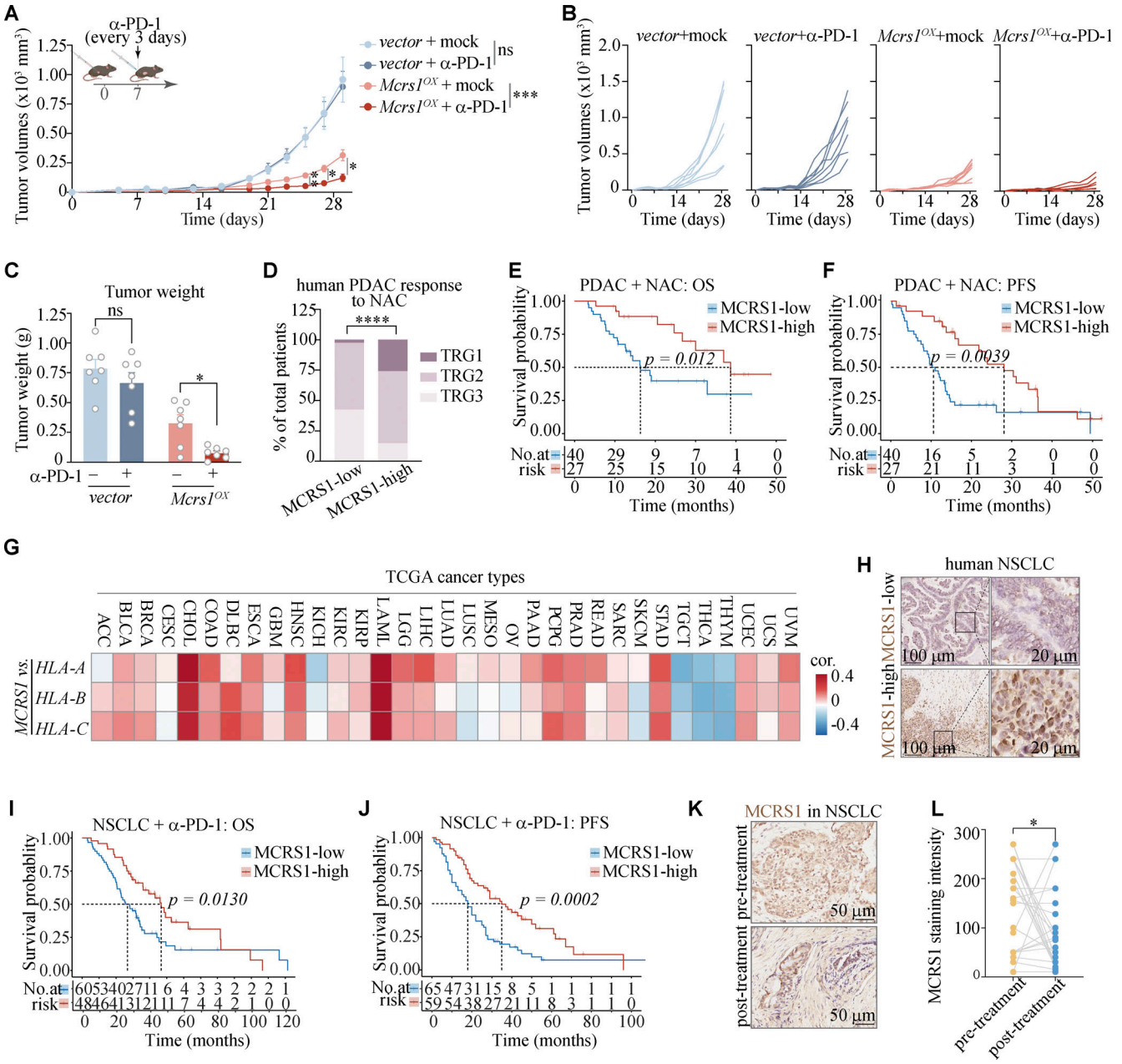

Figure 7. **MCRS1 sensitizes α-PD-1 immunotherapy in mice and humans. (A)** The tumor growth curve of control and *Mcrs1*^{OX} tumors treated with an α-PD-1 antibody (n = 7 for all groups; presented as means ± SEM; ns, not significant, P ≥ 0.05; *, P < 0.05; **, P < 0.01; ***, P < 0.001; two-way ANOVA with Sidak's multiple comparisons test; N = 2 independent experiments). Illustration was created with https://BioRender.com. **(B)** Spider plots showing tumor growth in individual mice as in A. **(C)** Tumor weights at the point of sacrifice (n = 7 for all groups; presented as means ± SEM; ns, not significant, P ≥ 0.05; *, P < 0.05; two-way ANOVA with Sidak's multiple comparisons test; N = 2 independent experiments). **(D)** Tumor responses to NAC of PDAC patients with different MCRS1 levels, determined by histological evaluation (n = 40, 27 for MCRS1-low and MCRS1-high groups, respectively; ****, P < 0.0001; Chi-square test). **(E)** Overall survival (OS) of PDAC patients with different MCRS1 levels after NAC treatment (n = 40, 27 for MCRS1-low and MCRS1-high groups, respectively; Kaplan–Meier test). **(F)** Progression-free survival (PFS) of PDAC patients with different MCRS1 levels after NAC treatment (n = 40, 27 for MCRS1-low and MCRS1-high groups, respectively; Kaplan–Meier test). **(G)** Correlation between *MCRS1* and MHC-I (*HLA-A,B,C*) expression in TCGA cancer types. **(H)** Representative IHC images showing high and low expression of MCRS1 (brown) in clinical samples of human NSCLC patients. Scale bars in the left panels = 100 μm; scale bars in the right panels = 20 μm. **(I)** Overall survival of NSCLC patients with different MCRS1 levels after α-PD-1 treatment (n = 60, 48 for MCRS1-low and MCRS1-high groups, respectively; Kaplan–Meier test). **(J)** Progression-free survival of NSCLC patients with different MCRS1 levels after α-PD-1 treatment (n = 65, 59 for MCRS1-low and MCRS1-high groups, respectively; Kaplan–Meier test). **(K)** Representative images showing MCRS1 levels in paired biopsies before and after α-PD-1 treatment (n = 25 for both groups). Scale bars = 50 μm. **(L)** MCRS1 expression in paired biopsies from the same patients before and after α-PD-1 treatment (n = 25 for both groups; *, P < 0.05; two-tailed paired t test).

recognize and clear cancer cells, deficiency in antigen presentation is one of the major causes of cancer immune evasion and resistance to immunotherapy (Galon and Bruni, 2019). Furthermore, PDAC bears a low mutational burden and suppresses antigen presentation (Maleki Vareki, 2018; Yamamoto et al., 2020a, 2020b; Zhong et al., 2020), underscoring insufficient $CD8^+$ T cell infiltration and limited responsiveness to ICB therapy.

Here, by focused CRISPRa screening, we identified MCRS1 as a key immune-sensitizing factor in pancreatic cancer cells by enhancing antigen presentation. Elevated MCRS1 expression was observed to correlate with increased cytotoxic T cell infiltration, both in mice and across clinical cohorts, and was significantly associated with extended survival and elevated efficacy to NAC in PDAC patients. Interestingly, the immune-sensitizing effect of MCRS1 appeared beyond pancreatic cancer, as high MCRS1 levels were associated with enhanced T cell activation in the majority of TCGA tumor types. In particular, we confirmed that elevated MCRS1 expression by cancer cells was predictive of an effective response to α-PD-1 therapy in an independent NSCLC cohort. These data collectively suggest that MCRS1 could sensitize cancer cells to T-cell immunity and thereby improve α-PD-1 efficacy.

MCRS1 is an understudied transcriptional regulator and lacks classical DNA-binding or enzymatic activities. MCRS1 has been primarily studied as a subunit of larger epigenetic regulatory complexes such as INO80 and NSL (Huang et al., 2022), with its own molecular function remaining largely elusive. In this study, we found that MCRS1 bound to the promoter/enhancer regions of MHC-I genes in mouse and human cells and elevated the expression of MHC-I genes. Notably, the regulation of MHC-I by MCRS1 was not dependent on known pathways such as NLRC5 or Interferon signaling (Kobayashi and van den Elsen, 2012; Parker et al., 2016; Pishesha et al., 2022), suggesting that MCRS1 may represent a new MHC-I activator. By enhancing antigen processing and presentation in cancer cells, MCRS1 sensitized cancer cells to $CD8^+$ T cell–mediated antitumor immunity.

We also started unraveling the molecular mechanism by which MCRS1 regulates MHC-I genes. By ChIP profiling of MCRS1 binding sites in the mouse genome and immunoprecipitation coupled with mass spectrometry (IP-MS) identification of MCRS1-interacting partners, we found that MCRS1 interacted with the transcription factor and chromatin organizer YY1 and co-occupied the genomic loci of many genes. In agreement with the fact that YY1 is recently recognized as a key chromatin organizer and that the chromatin organization is crucial for gene regulation (Weintraub et al., 2017), we showed that MCRS1 and YY1 coordinately regulated the chromatin accessibility and expression of target genes, including the MHC-I genes. Remarkably, overexpression of YY1 in pancreatic cancer cells also upregulated MHC-I genes, phenocopying that of MCRS1. Conversely, knockout YY1 in MCRS1-overexpressing cells ablated MHC-I upregulation by MCRS1 and consequently diminished the immune-sensitizing effects of MCRS1, resulting in decreased T cell activation and aggravated tumor growth in vivo. Of note, the dependence on YY1 in MCRS1-mediated immune sensitization agrees with previous reports concerning the tumor-suppressing effect of YY1 in pancreatic cancer (Zhang et al., 2014, 2017).

In summary, our study reveals MCRS1 as a new regulator of MHC-I–mediated antigen presentation, thereby transcriptionally overcoming the suppression of antigen presentation by cancer cells. Elevated MCRS1 could thus sensitize cancer cells, not only pancreatic cancer but also potentially other cancer types such as NSCLC, to T cell–mediated immunity and improve the efficacy of α-PD-1 immunotherapy. Therefore, MCRS1 could serve as an independent prognostic marker for patient stratification and predicting responses to α-PD-1 immunotherapy. Furthermore, given the technological advances in gene delivery and small molecule-mediated manipulation of gene expression (Ascic et al., 2024; Gourisankar et al., 2023; Kabir et al., 2024), MCRS1 may also be therapeutically manipulated in cancer to improve the efficacy of immunotherapy against the intractable disease.

Limitations of the study

As MCRS1 represents a new regulatory mechanism in tumor antigen presentation, further studies are warranted to investigate detailed mechanisms concerning the regulation and mode of action of MCRS1. For instance, it has been shown that *MCRS1* expression is upregulated in human pancreatic cancer (Huang et al., 2022), suggesting that it may function as a cell defense mechanism against tumorigenesis by engaging immune surveillance. However, it is not yet known whether MCRS1 is regulated in a cell-intrinsic manner as a response to tumor transformation or induced by extrinsic factors in the tumor microenvironment. In addition, our current screening mainly focuses on the interaction between primed effector T cells and tumor cells, mimicking the situation in the tumor. It would be intriguing to examine whether other factors would impact the priming of T cells by tumor antigens in the draining lymph nodes, which would provide another intervention opportunity to improve immunotherapy. Lastly, although we have observed the association between high MCRS1 expression and enhanced T cell activation in the majority of TCGA tumor types and confirmed the favorable effects of MCRS1 in PDAC and NSCLC patients, additional research efforts are required to elucidate whether MCRS1 could exert similar effects in other cancer types and whether it could function in a "pan-cancer" manner.

Materials and methods

Mice

Male and female *C57BL/6J* (RRID:IMSR_JAX:000664) and *Ifnar1*$^{-/-}$ (C57BL/6NCya-Ifnar1em1/Cya) mice were purchased from Shanghai Institutes for Biological Sciences (SLAC) and Cyagen Biosciences (C001268), respectively. *Ifnar1*$^{-/-}$ mice were back-crossed to *C57BL/6J* once and maintained as homogygous-to-omogygous breeding. *Pmel-1* (RRID:IMSR_JAX:005023, B6.Cg-Thy1^a/CyTg[TcraTcrb]8Rest/J) and OT-I (RRID:IMSR_JAX:003831, C57BL/6-Tg(TcraTcrb)1100Mjb/J) mice were obtained from the Jackson Laboratory and maintained by breeding to *C57BL/6J* mice. *Tcrb*$^{-/-}$;*Tcrd*$^{-/-}$ double knockout mice were

derived by crossing stock strains (RRID:IMSR_JAX:002118, B6.129P2-Tcrb^{tm1Mom}/J; RRID:IMSR_JAX:002120, B6.129P2-Tcrd^{tm1Mom}/J) of the Jackson Laboratory that have been extensively backcrossed to *C57BL/6J*. Mice of both sexes were used for experiments and were typically 6–12 wk old and weighed between 25 and 30 g. Mice were maintained under 12 h light:12 h dark cycles and fed ad libitum in the specific pathogen–free animal facilities of Fudan University. All mice were randomized before treatment and tumor assessment was conducted in a blinded manner. Mice were euthanized with 50 mg/kg pentobarbital sodium administered via intraperitoneal injection before tissue collection. All described experimental procedures were approved by the Institutional Animal Care and Use Committees (IACUC) of Fudan University (IDM2021001, IDM2024025).

Cell lines

The HT cell line was derived from the spontaneous pancreatic cancer tissues of *p48Cre*; *LSL-Kras^{G12D}*; *p53$^{L/+}$* mice under the B6 background and was a generous gift from Dr. Haoqiang Ying at the MD Anderson Cancer Center. HEK-293T (RRID:CVCL_0063) was purchased from the American Type Culture Collection (CRL-3216; ATCC). HT cells were grown in Roswell Park Memorial Institute 1640 (RPMI-1640, 350-005-CL; WISENT) media, and HEK-293T in Dulbecco's modified Eagle's medium (DMEM, 319-005; WISENT). All media were supplemented with 10% FBS (086-150; WISENT) and 100 IU/ml Penicillin-Streptomycin (450-201-EL; WISENT). Cells were maintained in a humidified incubator (NuAire) at 37°C with 5% CO_2 and were routinely checked for *Mycoplasma* with a Byotime Mycoplasma Detection Kit (C0298M), ensuring that all cells remained free from Mycoplasma contamination throughout the study.

Generation of the HT$^{dCas9\text{-}VPR}$ cell line

The coding sequences of *dCas9-VPR* were amplified from SP-dCas9-VPR (RRID:Addgene_63798, 63798; Addgene) and inserted into a pCAG-ires-iRFP plasmid (RRID:Addgene_47884, 47884; Addgene). The resulting plasmid was transfected into HT cells with Fugene HD (E2311; Promega). Cells were then sorted twice with a FACSAria Flow Cytometer (BD Biosciences) according to the iRFP fluorescence and seeded into 96-well plates with an average of 0.3 cells/well. Individual clones were allowed to grow for 3 wk and examined for iRFP fluorescence by flow cytometry. Clone #6 was selected and expanded in culture for further experiments.

To test gene activation in the CRISPRa systems in the HT$^{dCas9\text{-}VPR}$ cells, three sgRNAs targeting the mouse *Leptin* gene were obtained from the Mouse Genome-wide CRISPRa-v2 Libraries (RRID:Addgene_83996, 83996; Addgene) and cloned into a modified pLentiCRISPR v2 vector (RRID:Addgene_52961, 52961; Addgene) with *Cas9* removed. sgRNA plasmids were transfected into HEK293T cells together with pMD2.G (RRID:Addgene_12259, 12259; Addgene) and psPAX2 (RRID:Addgene_12260, 12260; Addgene) to produce lentivirus, which was used to transduce HT$^{dCas9\text{-}VPR}$ cells. Cells were harvested 48 h later and RNA was extracted with an RNeasy Mini Kit (74014; Qiagen) and reverse-transcribed with a QuantiTect RT Kit (205311; Qiagen) following the manufacturer's instructions. *Leptin* expression was determined by quantitative PCR (qPCR) (Lu et al., 2015) and the Fast SYBR Green Master Mix (4385616; Thermo Fisher Scientific) on an Applied Biosystems 7500HT system (Thermo Fisher Scientific).

HT$^{dCas9\text{-}VPR}$ screening

The Mouse Gene Expression Subpool CRISPRa-v2 Library (RRID: Addgene_84002, 84002; Addgene) was transfected into HEK-293T cells with pMD2.G (RRID:Addgene_12259) and psPAX2 (RRID:Addgene_12260) to produce lentivirus, which was used to transduce the HT$^{dCas9\text{-}VPR}$ cells. TagBFP^{+} cells were sorted with a FACSAria Flow Cytometer (BD Biosciences) according to blue fluorescence intensities.

Spleens were harvested from 6–8-wk-old *Pmel-1* mice and dissociated into single cells. CD8^{+} T cells were purified with the Untouched Mouse CD8 T cell Kit (11417D; Thermo Fisher Scientific) and cultured at a density of 4 × 10^{6} cells/ml in the presence of 1 uM of the hgp100(25-33) peptide (RP20344; Genscript) and 20 U/ml recombinant mouse IL-2 (575408; Biolegend) in RPMI-1640 media supplemented with 10% FBS (10098-148; GIBCO), 1 mM Sodium Pyruvate (600-110-EL; WISENT), 1× non-essential amino acid (321-001-EL; WISENT), 2 mM L-Glutamine (609-065-EL; WISENT), 55 uM 2-Mercaptoethanol (β-ME, 21985023; GIBCO) and 1× Penicillin-Streptomycin (450-201-EL; WISENT). An equal volume of fresh medium was added on Day 3. *Pmel-1* CD8^{+} T cells were harvested on Day 5, washed twice with Dulbecco's phosphate-buffered saline (DPBS, 211-410-XK; WISENT), and rested overnight in complete RPMI media.

sgRNA-transduced HT$^{dCas9\text{-}VPR}$ cells were digested off culture dishes, washed twice with DPBS, and incubated with 1 μM of the hgp100 (25–33) peptide in RPMI media for 1 h at 37°C to pulse loading of hgp100. After being washed twice with DPBS to remove unbound hgp100, 1 × 10^{7} cells/ml HT$^{dCas9\text{-}VPR}$ cells were seeded into a 10-cm culture dishes as the killing group while HT$^{dCas9\text{-}VPR}$ cells without hgp100 loading were used as the mock group. HT$^{dCas9\text{-}VPR}$ cells were incubated for 4 h before *Pmel-1* CD8^{+} T cells were added at a ratio of 1:1, which roughly provided 1,000× library coverage (1 × 10^{7} cells for ~10^{4} sgRNAs). After 18-h co-culture, T cells were washed off with DPBS, and residual HT$^{dCas9\text{-}VPR}$ cells were recovered in fresh media to allow expansion. The killing screen procedure was carried out another two times.

At the end of the third screen, surviving HT$^{dCas9\text{-}VPR}$ cells were collected and genomic DNA was extracted with the Quick-DNA Midiprep Plus Kit (D4075; Zymo). sgRNAs were amplified by PCR as previously described (Gilbert et al., 2014; Horlbeck et al., 2016) and sequenced on a HiSeq 2000 Sequencer (Illumina). Sequencing reads were processed with the MAGeCKFlute (RRID:SCR_025016, v.2.2.0) (Li et al., 2014) and ScreenProcessing (v.0.2) (Horlbeck et al., 2016) pipelines.

Cell line engineering

The coding sequences of mouse *Mcrs1* were amplified from the pancreas cDNA with specific primers and cloned into the pCD513B lentiviral vector (SBI) with the FLAG tag at the N terminus. Sequences were verified with Sanger sequencing.

Lentiviral plasmids were transfected into HEK-293T cells together with pMD2.G (RRID:Addgene_12259) and (RRID:Addgene_12260), and culture supernatant with lentivirus was used to transduce HT or other cell lines. GFP$^+$ cells were sorted twice with a FACSAria Flow Cytometer (BD Biosciences) to obtain stable cell lines (vector control/*pCD513B* and *Mcrs1*^{OX}). Another cell line expressing *3xFlag-Mcrs1* under the control of the *EF1a* promoter was similarly generated.

To generate *Ovalbumin*-expressing cell lines, *Ovalbumin* coding sequences were cloned into a lentiviral vector (174-Ova), which encodes a *CD90.1* marker. Lentivirus was packaged as above and used to transduce vector control/*pCD513B* or *Mcrs1*^{OX} cells. Cells were stained with an anti-CD90.1 antibody (RRID:AB_2562644, 202537, clone OX-7; Biolegend) antibody and sorted with a FACSAria Fusion Flow Cytometer (BD Biosciences).

To generate *Mcrs1*^{KO} cell lines, sgRNAs targeting *Mcrs1* or *Gt(ROSA)26Sor* were cloned into a modified pLentiCRISPR v2 vector (RRID:Addgene_52961, 52961; Addgene), pJFXY174, which encodes *Cd90.1*. Lentivirus was packaged as above and used to transduce wild-type HT cells. Cells were stained with an anti-CD90.1 antibody (RRID:AB_2562644, 202537; BioLegend) and sorted with a FACSAria Fusion Flow Cytometer (BD Biosciences). Sorted cells were seeded into 96-well plates with an average of 0.3 cells/well. Individual clones were allowed to grow for 3 wk and examined for MCRS1 knockout by western blot. Clone #P3F3 was selected and expanded in culture for further experiments.

In vitro cytotoxicity assay

CD8$^+$T cells were isolated from the spleen and lymph nodes of *Pmel-1* and OT-I mice and stimulated with 5 μM of human gp100 (25–33) peptides (HY-P1585A; MCE) and 1 μM of SIINFENKL peptides (13-5743-82; Thermo Fisher Scientific), respectively, for 4 days and rested overnight in fresh media without antigenic peptides.

To load the ovalbumin antigen, cells were pulsed with 1 μM of human gp100 (25–33) peptides (HY-P1585A; MCE) or SIINFENKL peptides (13-5743-82; Thermo Fisher Scientific) and incubated at 37°C for 1 h. After being washed twice with DPBS. For separate tumor culture, vector control and *Mcrs1*^{OX} tumor cells were resuspended in complete RPMI-1640 media at a cell density of 1 × 10^6 cells/ml. For mixed tumor cell culture, vector control and *Mcrs1*^{OX} tumor cells were labeled with 0.5 and 5 μM of CellTrace Violet (C34557; Thermo Fisher Scientific), respectively, at 37°C for 20 min. Labeling was stopped by adding 12 ml of cold complete RPMI-1640 media and incubating at room temperature for 5 min. Tumor cells were then washed twice with cold complete RPMI-1640 media, followed by pulsing with antigenic peptides. Vector control and *Mcrs1*^{OX} cells were then mixed at a 1:1 ratio with the final cell density adjusted to 1 × 10^6 cells/ml.

For the in vitro cytotoxicity assay, tumor cells were seeded into a U-bottomed 96-well plate at a density of 100,000 cells/well and incubated with *Pmel-1* or OT-I T cells at different ratios (effector:target = 0:1, 0.25:1, 0.5:1, 1:1…) at 37°C for 12 h (*Pmel-1*) or 24 h (OT-I). Cells were then washed with DPBS, digested with Trypsin (325-043-CL; WISENT), and resuspended FACS buffer (DPBS, 0.2% BSA, 2 mM EDTA) with 1 μl of CountBright Absolute Counting Beads (C36950; Thermo Fisher Scientific). Cells were analyzed with an LSRFortessa flow cytometer (BD Biosciences), with dead cells discriminated by staining with 7-AAD Viability Dye (00-6993-50; eBiosciences). Control and *Mcrs1*^{ox} tumor cells were differentiated by low and high staining of CellTrace Violet (C34557; Thermo Fisher Scientific), respectively, in mixed tumor culture experiments. Data analysis was performed with FlowJo (RRID:SCR_008520, v.10.5.3; BD Biosciences).

IFN-γ ELISA

IFN-γ was detected with the Mouse IFN-γ ELISA Kit (430801; BioLegend), following the manufacturer's instructions. Briefly, the culture supernatant from in vitro cytotoxicity assays for vector control and *Mcrs1*^{OX} tumor cells was harvested at the end of the experiments. The supernatant from *Pmel-1* T cell co-culture was diluted by 500 folds with Assay Diluent Buffer (421203; BioLegend) and that from OT-I T cell co-culture was diluted by 1000 folds. 50 μl of standards or samples were added to each well for IFN-γ detection. Absorbance at 450 nm was measured with 570 nm as a reference using a SpectraMax i3x plate reader (Molecular Devices).

Mouse tumor models

Tumor cells (1 × 10^6 cells in 200 μl DPBS) were subcutaneously injected into the flanks. Tumor growth was monitored every 3–4 days and tumor diameters were measured with a caliper. Tumor volumes were calculated as $(Length \times Width^2)/2$. Mice were humanely sacrificed when tumor volumes exceeded 1,500 mm^3 in compliance with IACUC policies. For the orthotopic tumor model, 500,000 cells were suspended in 30 μl pre-cold HBSS (311-513; WISNET) and slowly injected into the pancreases of female C57BL/6J mice with U-40 syringes after anesthetization. 3 wk later, mice were killed and tumor tissues were dissected, weighed, and fixed in 4% paraformaldehyde (PFA).

For α-PD-1 treatment, mice were subcutaneously inoculated with tumor cells as described above. 200 μg of α-PD-1 antibody (IBI308; Innovent Biologic) or DPBS was injected intraperitoneally when tumors reached a size of 20 mm^3 on Day 5. Mice were treated every 3 days with tumor sizes routinely monitored. All injections were performed at 10:00 AM using a 1 ml syringe with a 26-gauge needle.

Bulk RNA-seq

Control and *Mcrs1*^{OX} cells or tumor tissues were harvested from cell culture or tumor-bearing mice, respectively, and processed with an RNAsimple total RNA kit (DP419; TIANGEN) according to the manufacturer's instructions. The RNA integrity was examined with a Qsep 100 (BiOptic). Total RNA was subjected to polyA selection and library preparation with a TruSeq Stranded mRNA LT Kit (RS-122-2120; Illumina). Samples were barcoded and run on a HiSeq4000 sequencer (Illumina) with 150/150 bp paired-end reading.

Raw fastq files were filtered and trimmed with fastp (RRID:SCR_016962, v.0.22.0) and then aligned with HISAT2

(RRID:SCR_015530, v.2.2.1) to the GRCm38 reference genome with default settings. Mapped reads were quantified with featureCounts (RRID:SCR_012919, v.2.0.1) using the GENCODE (RRID:SCR_014966) M25 gtf file. Data normalization and differential gene expression analysis were performed with R (RRID:SCR_001905, v.4.2.1) and the *limma* (RRID:SCR_010943, v.3.54.0) package. The normalized count table was fed to the GSEA software (RRID:SCR_003199,v.4.3.2, Broad Institute) for gene set enrichment analysis. Immune cell fractions were estimated with CIBERSORTx (RRID:SCR_016955) at https://cibersortx.stanford.edu/ following the authors' instructions.

RT-PCR

RNA was reversely transcribed with a HiScript III first Strand cDNA Synthesis Kit (+gDNA wiper) (R312; Vazyme) following the manufacturer's instructions. cDNA was diluted fivefold with sterile H_2O and used for qPCR with the 2xChamQ Universal SYBR qPCR Master Mix (Q711; Vazyme) on a Quant Studio3 Real-Time PCR System (Thermo Fisher Scientific). Gene expression was normalized to β-actin and was calculated with the $2^{-\Delta\Delta Ct}$ method. Primers used are listed in Table S5.

TIL analysis

Tumor masses were dissected from mice and cut into ∼1 mm^3 pieces, followed by enzymatic digestion with 0.25 mg/ml Collagenase Type IV (17104-019; GIBCO) and 0.1 mg/ml DNaseI (B300065; Sangon Biotech) at 37°C for 30 min. The cell suspension was overlaid onto 32.5% Percoll Plus (17544501; Cytiva) and centrifuged at 800 *g* for 20 min at room temperature. TILs were harvested at the bottom of conical tubes and red blood cells were removed with the RBC Lysis Buffer (00-4300-54; Thermo Fisher Scientific).

For cytokine production analysis, isolated cells were stimulated with 50 ng/ml phorbol 12-myristate-13-acetate (79346; Sigma-Aldrich), 1 µM ionomycin (407952; Sigma-Aldrich), and 5 ng/ml brefeldin A (203729; Sigma-Aldrich) for 3 h at 37°C. Cells were then blocked with an anti-CD16/CD32 antibody (RRID:AB_394657, 553142; BD, clone 2.4G2) on ice for 30 min and stained with ZombieNIR (423105; Biolegend) and antibodies against CD45 (RRID:AB_893344, 103131; Biolegend), CD3ε (RRID:AB_842788, 12-0033-81; Thermo Fisher Scientific, clone 500A2), CD4 (RRID:AB_2561388, 103131; Biolegend, clone RM4-5) and CD8α (RRID:AB_312745, 100706; Biolegend, clone 53-6.7). After washing three times, cells were fixed and permeablized with the transcription factor staining kit (00-5523-00; eBioscience), followed by intracellular staining with an antibody against IFN-γ (RRID:AB_2295770, 505826; Biolegend, clone JES6-5H4). An LSRFortessa flow cytometer (BD Biosciences) was used for data acquisition, followed by data analysis with FlowJo (RRID:SCR_008520).

For surface effector/memory analysis, TILs were surfaced blocked with an anti-CD16/CD32 antibody (RRID:AB_394657, 553142; BD, clone 2.4G2) and stained with ZombieNIR and antibodies against CD3ε (RRID:AB_842788, 12-0033-81; Thermo Fisher Scientific, clone 500A2), CD4 (RRID:AB_2561388, 103131; Biolegend, clone RM4-5), CD8α (RRID:AB_312745, 100706; Biolegend, clone 53-6.7), KLRG1 (RRID:AB_10643582, 138410; Biolegend, clone 2F1/KLRG1), and CD127 (RRID:AB_1937216, 135012; Biolegend, clone IL-7RA). Cells were analyzed above.

Sample preparation for scRNA-seq and scTCR-seq

TILs were isolated as above, blocked with TruStain FcX (RRID:AB_1574973, 101319; Biolegend), and stained with anti-TCRβ (RRID:AB_2562562, 109230; Biolegend, clone H57-597) and CD90.2 (RRID:AB_313176, 105305; Biolegend, clone 30-H12) for 30 min at 4°C. Cells were then washed twice and $TCR\beta^+$ $CD90.2^+$ cells were sorted with a FACSAria Fusion Flow Cytometer (BD Biosciences), with dead cells excluded as $DAPI^+$. Sorted cells were pelleted, stained with TotalSeq Hashtags (vector control: RRID:AB_2800693, 155861; Biolegend; $Mcrs1^{OX}$: RRID:AB_2800694, 155863; Biolegend), washed, and resuspended at a density of 1×10^3 cells/ml in 0.04% BSA buffer. Hashtagged cells were pooled and loaded onto a Chromium Controller (10x Genomics) for single-cell encapsulation. The cDNA library was generated with the Chromium Single Cell 3′ v2 Reagent Kits (10X Genomics) and subsequently sequenced on a NovaSeq 6000 sequencer (Illumina) with a 150/150 bp paired-end run.

scRNA-seq and scTCR-seq data processing

Raw fastq files were processed with Cellranger (RRID:SCR_023221, v.7.1.0) by aligning to the mm10 reference genome and the GRCm38 VDJ reference for gene expression and TCR clonotype analysis, respectively. Cell hashing barcode sequences were also aligned for demultiplexing. The gene expression matrix and cell hashing barcode matrix were integrated with Seurat (RRID:SCR_016341, v.4.0.5) in RStudio Server (RRID:SCR_000432) running R (RRID:SCR_001905, v.4.1.2) for further analysis. Data were filtered so that only cells with >200 expressed genes and <5% mitochondrial mRNA were retained. In this way, we obtained high-quality data for 665 and 1,541 cells in the vector control and $Mcrs1^{OX}$ group, respectively. After normalization and scaling, data were subject to principal component analysis using the top 2,000 variable genes. The first 10 principal components were used for unsupervised clustering with the shared nearest neighbor approach and for constructing a Uniform Manifold Approximation and Projection (UMAP) for data visualization.

Cell types of individual clusters were identified according to the expression of canonical markers and lymphocytes (T cells and NK cells) were extracted for refined clustering. Pseudo-bulk analysis was performed with DESeq2 (RRID:SCR_015687, v.1.38.2) in Seurat (RRID:SCR_016341, v.4.0.5), with differentially expressed genes identified by $\log_2$(fold change) >1.5 and adjusted P value <0.05. Pseudotime analysis was performed with Monocle2 (RRID:SCR_016339, v.2.26.0). The Gini Index of TCR clonotypes was calculated with the R package ineq (v.0.2-13).

MHC-I detection by flow cytometry

Vector control, $Mcrs1^{OX}$ tumor cells or *Ovalbumin*-expressing cells were digested with Trypsin (325-043-CL; WISENT) and resuspended in FACS buffer. To detect total MHC-I, cells were stained with an MHC Class I (H-2Kb) antibody (RRID:AB_1311283, 17-5958-80; Thermo Fisher Scientific, clone AF6-88.5.5.3). To detect ovalbumin presented by MHC-I on the cell surface,

Ovalbumin-expressing cells were stained with an anti-mouse H-2K^b bound to SIINFEKL antibody (RRID:AB_11219402, 141605; BioLegend, clone 25-D1.16). Cells were analyzed with LSRFortessa flow cytometer (BD Biosciences) and data were processed with FlowJo (RRID:SCR_008520).

T cell proliferation assay

CD8$^+$ T cells were purified from the spleen and lymph nodes of OT-I transgenic mice as before and labeled with 5 μM CellTrace Violet (C34557; Thermo Fisher Scientific). *Ovalbumin*-expressing control and *Mcrs1*^{ox} tumor cells were trypsinized and resuspended in complete RPMI-1640 media at a cell density of 1 × 10^6 cells/ml. 50,000 tumor cells and 50,000 OT-I T cells were mixed and seeded into a U-bottomed 96-well plate. T cells were analyzed 72 h later with an LSRFortessa flow cytometer (BD Biosciences). Data were then processed with FlowJo (RRID: SCR_008520), and T cell proliferation was assessed by the dilution of CellTrace Violet.

Co-immunoprecipitation and mass spectrometry

HT cells stably expressing *Flag-Mcrs1* or pCD513B vector control were grown on 15-cm culture dishes until reaching 95% confluency. Cells were harvested, washed three times with ice-cold DPBS, and 2.5 × 10^7 cells were resuspended in 2 ml of the radioimmunoprecipitation assay (RIPA) lysis buffer pH7.4, supplemented with 1 mM PMSF (A100754; BBI), 1 μg/ml Aprotinin (A100429; BBI), 1 μg/ml Leupeptin (A600580; BBI), 1 μg/ml Pepstatin (A610583; BBI), 1 mM Na_3VO_4(A600869; BBI), 10 mM NaF (A500850; BBI), 5 mM nicotinamide (72345; Sigma-Aldrich), 0.5 mM trichostatin A (A606777; BBI). Cells were incubated at 4°C for 20 min with gentle shaking (200 rpm/min), and cell lysates were cleared by centrifuging at 13,000 rpm at 4°C for 20 min. The lysis supernatant (~ 1.9 ml) was harvested and incubated with 20 μl of anti-FLAG Affinity Gel (51326C001; GNI) and rotated for 4 h at 4°C. Beads were pelleted by centrifuging at 3,000 rpm for 3 min at 4°C, followed by washing four times with RIPA buffer. Immunoprecipitated proteins were eluted with SDS buffer by boiling at 95°C for 10 min. The eluates were run on 10% SDS-PAGE gel and stained with Coomassie Blue for mass spectrometry.

Mass spectrometry was performed with a timsTOF Pro mass spectrometer (Bruker) coupled to Nanoelute (Bruker Daltonics). Proteins were identified with Mascot and analyzed with STRING (RRID:SCR_005223, v.12.0) for protein–protein interaction networks.

Western blot

For whole-cell lysates, cells were lysed with RIPA buffer supplemented with 1 mM PMSF (BBI, A100754) and 1× protease inhibitor cocktail (K1007; APExBio). Protein concentrations were measured with the bicinchoninic acid (BCA) assay (CW0014; CWBio). Samples were mixed with 5× SDS loading buffer, heated at 95°C for 10 min, and loaded onto 10% SDS-PAGE gels together with 5 μl of protein ladder (Epizyme WJ103, 1610374; Bio-Rad, or 26616; Thermo Fisher Scientific). Proteins were then transferred to polyvinylidene fluoride (PVDF) membranes (IPVH00010; Millipore), which were then blocked with 5% non-fat milk with 0.1% Tween-20 (TBS-T). Primary antibodies such as anti-β-ACTIN (RRID:AB_2801259, GB11001; Servicebio), anti-MCRS1 (RRID:AB_2143116, 1:1,000, 11362-1-AP; Proteintech), and anti-YY1 (RRID:AB_2737053, 1:10,00066281-1-AP; Proteintech) were incubated with PVDF membranes overnight at 4°C, followed by incubation with HRP-conjugated secondary antibodies for 1 h at room temperature. Proteins of interest were visualized with ECL reagents (P0018M; Beyotime) in a Chemi-Scope 2100 chemiluminescence detection system (CLINX).

ChIP-seq assay

Six million cells were washed with DPBS and cross-linked with 20 ml of fresh 1% formaldehyde (F79-500; Thermo Fisher Scientific) for 15 min with gentle mixing at room temperature. The cross-link reaction was quenched with 0.125 M of glycine at room temperature for 5 min. Cells were then washed twice with ice-cold PBS and collected by centrifuging at 1,000 *g* for 5 min at 4°C. Cells were resuspended in 200 μl of sonication buffer (20 mM Tris pH 8.0, 2 mM EDTA, 0.5 mM EGTA, 1× protease inhibitors [K1007; APExBio], 0.5% SDS, and 1 mM PMSF) and incubated on ice for 10 min, followed by sonication with a Qsonica Q800R2 sonicator at 70% amplitude. Chromatin was sheared with 15 s on: 45 s off cycles for a total of 15 min and centrifuged at maximum speed (16,000 *g*) for 10 min at 4°C. Cleared chromatin was transferred into a new microcentrifuge tube, and 10% was taken out as Input and stored at −20°C. For each ChIP reaction, 25 μl of Protein A beads (10001D; Thermo Fisher Scientific) and 25 μl of Protein G beads (10003D; Thermo Fisher Scientific) were mixed and blocked with 1 ml of blocking buffer (DPBS + 0.5% BSA). After washing, beads were resuspended in 300 μl of blocking buffer and incubated with 4 μg of anti-MCRS1 antibody (RRID:AB_2143116, 11362-1-AP; Proteintech) for 6 h at 4°C with gentle rotation. Clear chromatin was then added to the beads-antibody complex and incubated overnight at 4°C with gentle rotation. The next day, beads were washed three times with the LiCl wash buffer (50 mM Tris-HCl pH 8.0, 1 mM EDTA, 500 mM LiCl, 1% NP40, and 0.7% sodium deoxycholate) and twice with 1× Tris-EDTA buffer. Beads were then mixed with 200 μl reverse-crosslinking buffer (1% SDS, 0.1 M $NaHCO_3$) and incubated at 65°C on a thermomixer at 950 rpm for 10 h, followed by the addition of 20 mg/ml proteinase K (10401ES60; Yeasen) and incubation at 65°C for 2 h. ChIP DNA was purified with the HiPure Gel DNA Mini Kit (D2111; Magen) and used for library construction with VAHTS Universal DNA Library Prep Kit for Illumina V3 (ND607; Vazyme) following the manufacturer's manual. Samples were then sequenced with a NovaSeq6000 sequencer (Illumina) with 150/150 bp paired-end reading.

ChIP-seq data processing

Raw fastq files were filtered and trimmed with fastp (RRID: SCR_016962, v.0.22.0) and then aligned with BOWITE2 (RRID: SCR_016368, v.2.5.0) to the GRCm38 reference genome using parameters –local --very-sensitive --no-mixed --no-discordant. MACS2 (RRID:SCR_013291, v.2.2.7.1) was used for peak calling with the "-f BAMPE --broad -P 0.001" settings and HOMER (RRID:SCR_010881, v.4.11) was used for motif discovery. For

ChIP-seq data of HepG2 cells, raw fastq files were downloaded from GEO with accession number GSE97411. Reads were aligned to the hg19 reference genome and analyzed as above. Bam files were converted to bigwig files by the deepTools (RRID: SCR_016366, v.3.5.1) subcommand bamCoverage with the following parameters: --binSize 10 --normalizeUsing reads per kilobase per million mapped reads (RPKM).

ATAC-seq

ATAC-seq was performed with a Hyperactive ATAC-Seq Library Prep Kit for Illumina (TD711; Vazyme) following the manufacturer's instructions. Briefly, 50,000 cells were washed twice with 50 µl of Buffer TW and resuspended in 50 µl of Lysis Buffer. After incubating on ice for 5 min, nuclei were collected by centrifuging at 500 *g* for 10 min at 4°C and resuspended in 50 µl of Transposition Mix (16.5 µl of TW buffer, 0.5 µl of 10% Tween-20, 0.5 µl of 1% Digitonin, 10 µl of 5× Tagment buffer, 4 µl of Tranposase, 18.5 µl of Nuclease-free H_2O), followed by incubation at 37°C for 30 min. After incubation, 5 µl of Stop Buffer was added and incubated at room temperature for 5 min. DNA fragments were purified with 100 µl of DNA Extract Beads and eluted in 26 µl of Nuclease-free H_2O. To prepare the sequencing library, 20 µl of DNA was mixed with 30 µl of 2× Buffer CAM, 5 µl of N5XX index primer, and 5 µl of N7XX index primer for PCR amplification. The DNA library was cleaned with the ATAC DNA Clean Beads and sequenced with a HiSeq4000 sequencer (Illumina) with 150/150 bp paired-end reading.

Data processing for ATAC-seq

Raw fastq files were filtered and trimmed with fastp (RRID: SCR_016962, v.0.22.0) and then aligned with BOWITE2 (RRID: SCR_016368, v.2.5.0) to the GRCm38 genome using parameters "–local --very-sensitive --no-mixed --no-discordant". Meanwhile, fastq files were also aligned to the *E. coli* reference genome using BOWITE2 to detect spike-in DNA for sequencing depth normalization. Peak calling was performed with MACS2 (RRID:SCR_013291, v.2.2.7.1) with the following settings: -f BAMPE --nomodel -s 1 --shift 75 --extsize 150 -q 0.01. Peaks detected in all replicates were considered as consensus peaks and used for downstream analysis. Reads fall-in peaks were counted manually using BEDTools (RRID:SCR_006646, v.2.30.0) and differential chromosome accessibility analysis was performed by MAnorm (RRID:SCR_010869).

For Track visualization, Bam files were converted to bigwig files by the bamCoverage subcommand of Deeptools (RRID: SCR_016366, v.3.5.1) with the binSize set at 10, followed by importing into the IGV Genome Browser (RRID:SCR_011793, v.2.16.0) for visualization. For multi-omics data, data from different experiments were adjusted to the same scale during visualization.

TCGA analysis

TCGA transcriptome data (HTSeq-Counts) were downloaded from the UCSC Xena website (https://xena.ucsc.edu) and normalized with counts per million mapped reads (CPM) in R, followed by $\log_2$ transformation. The T cell activation signature was defined by Singer et al. (2016). Pearson's correlation between the expression of individual candidate genes and the T cell activation signature was calculated in patient cohorts of various cancer types.

H&E staining

Mouse tissues were fixed in formalin and embedded in paraffin. Tissues were cut into 3-µm-thick sections with a HistoCore BIOCUT microtome (Leica). H&E staining was performed with an HistoCore CHROMAX ST automatic stainer (Leica), with hematoxylin (BA-4041; Baso) and eosin (BA-4022; Baso). Subsequently, slides were scanned using an Aperio CS2 (Leica) at 10× magnification and analyzed with the HALO digital pathology system (v3.3; Indica Labs).

Clinical specimens

Immunohistochemical staining for MCRS1 was performed on the tumor sections of patients with PDAC. Samples from the 704-case cohort were collected at Changhai Hospital of Navy Medical University (Shanghai, China) between 2016 and 2019. The study was approved by the Institutional Review Board of Navy Medical University (Approval number CHEC2024-109), with the written informed consent of all patients. No endocrine therapy, chemotherapy, or radiotherapy was given to subjects before surgery. Sample processing and IHC assessments were conducted as previously reported (Liu et al., 2016), and pathology scoring was performed by two independent pathologists. In brief, the proportion of positive cells was estimated and given a percentage from 1 to 100%. The average intensity of positively stained cells was given an intensity score from 0 to 3 (0 = no staining; 1 = weak; 2 = intermediate; and 3 = strong staining). The resulting pathology scores ranged from 0 to 300, with the median value of 120 used as the cutoff. A separate cohort with 67 post-neoadjuvant therapy surgical samples was obtained from Changhai Hospital of Navy Medical University (Shanghai, China) between 2018 and 2020, with all patients having received neoadjuvant therapy prior to surgery. Tumor responses to NAC were evaluated according to the pathological TRG scoring system: TRG 0, no residual tumor cells (also known as pathological complete response); TRG 1, single cells or small groups of tumor cells; TRG 2, residual tumor cells with desmoplastic response; and TRG 3, minimal evidence of tumor response.

To investigate the effect of MCRS1 on α-PD-1 therapy in NSCLC patients, an additional independent cohort comprising 107 cases was assembled at Changhai Hospital of Navy Medical University (Shanghai, China), spanning the years 2016–2021. All participants provided documented informed consent. Patients with intermediate to advanced NSCLC, ineligible for surgical resection, received combined chemotherapeutic and anti-PD-1 immunotherapeutic interventions. A total of 107 pretreatment biopsy specimens and 25 intra-treatment biopsy specimens were obtained via bronchoscopic puncture.

IHC staining

Human PDAC and NSCLC tissues were fixed in 4% PFA immediately after tissue collection, embedded in paraffin, and stored at 4°C in plastic block storage boxes. Samples were cut into 3-µm-thick sections as described above, followed by deparaffinization, rehydration, and antigen retrieval in the EDTA buffer

(pH9.0, ZLI-9069; ZSGB-BIO). Endogenous peroxidase activity was blocked by incubation with the peroxidase buffer (ZLI-9311; ZSGB-BIO) for 15 min. Non-specific antibody binding was blocked with goat serum (ZLI-9056; ZSGB-BIO) for 30 min at room temperature. Sections were then incubated with an anti-MCRS1 antibody (ab247013; Abcam) overnight at 4°C, followed by incubation with an HRP-conjugate secondary antibody (PV-6000; ZSGB-BIO) for 30 min at room temperature. The nuclei were stained with hematoxylin. Whole slides were scanned at 10× magnification with Aperio CS2 (Leica). For MCRS1 analysis, the HALO Image Analysis Software (v3.3, Indica Labs) was used to analyze digital histology images, with a three-tier scale (0: negative to weak; 1: moderate, 2: strong).

Multiplexed immunofluorescence staining

Sections were prepared and blocked as above, and stained with an AlphaTSA Multiplex Immunohistochemistry Kit (AXT37100031; AXB) following the manufacturer's instructions. For mouse tissues, the following antibodies were used: anti-MCRS1 (ab247013; Abcam), anti-CD8α (ab217344; Abcam), and anti-αSMA (RRID:AB_3095325, ZM-0003; ZSGB-BIO). For human tissues, the following antibodies were used: anti-MCRS1 (ab247013; Abcam), anti-YY1 (RRID:AB_10890662, ab109237; Abcam), anti-CD8α (RRID:AB_2890107, ZA-0508; ZSGB-BIO), and CK8/18 (ZMO315; ZSGB-BIO). DAPI (AXT9110000; AXB) was used for nuclei staining. Images were acquired with Zeiss Axioscan 7 and analyzed the HALO Image Analysis Software (v3.3; Indica Labs) was used for image analysis.

Statistical analysis

Animals were randomly assigned to treating groups and data collection was randomized. No data points were excluded from the analyses. No statistical methods were used to predetermine sample sizes but our sample sizes are similar to those reported in previous publications. Statistical analysis was performed with GraphPad Prism (RRID:SCR_002798, v.9.5.0), GSEA (RRID:SCR_003199,v.4.3.2), and R (RRID: SCR_001905, v.4.2.1) with packages specified in individual experiments. All dots represent biological replicates and all data are verified in at least two independent experiments with similar results.

Online supplemental material

Fig. S1 shows additional information on CRISPRa screening, including HT cell characterization, screening analysis with two different algorithms, and the association between MCRS1 expression and human PDAC disease status. Fig. S2 shows additional supportive data on the immune-sensitizing effect of MCRS1. Fig. S3 shows additional analysis of scRNA-seq data. Fig. S4 presents additional evidence on the regulation of MHC-I by MCRS1. Fig. S5 shows additional data on the MCRS1-YY1 axis in MHC-I regulation. Table S1 reports PDAC patient information in histological studies (Figs. 1 and S1). Table S2 shows the list of genes regulated by MCRS1, identified by integrative analysis of RNA-seq, ChIP-seq, and ATAC-seq. Table S3 reports PDAC patient information in the NAC study (Fig. 7). Table S4 reports NSCLC patient information in the anti-PD1 immunotherapy study (Fig. 7). Table S5 reports gene-specific primers for qPCR. Table S6 shows sgRNA sequences for CRISPR activation or knockout.

Inclusion and ethics statement

We support the inclusive, diverse, and equitable conduct of research.

Data availability

Raw and processed data of RNA-seq of cultured cells (GSE239358), RNA-seq of tumors (GSE239364), scRNA-seq (GSE239360), ChIP-seq (GSE239359), and ATAC-seq (GSE239357) related to Figs. 3, 4, 5, and 6 are openly available in the Gene Expression Omnibus (GEO, RRID:SCR_005012) under the Superseries GSE239365. Mouse strains are all commercially available. All other data are available in the main text or the supplementary materials. No custom code or software was generated in this study. Correspondence and requests for materials should be addressed to xiaofei_yu@fudan.edu.cn (X. Yu).

Acknowledgments

The authors want to thank Dr. Haoqiang Ying at the MD Anderson Cancer Center, Houston, TX, USA, for sharing the mouse pancreatic cancer cell line, Dr. Chen Dong at Westlake University and Dr. Yiran Zheng at Soochow University for help with mouse strains, and Dr. Kivanc Birsoy at the Rockefeller University for insightful discussions. The authors also thank the animal facilities of the State Key Laboratory of Genetic Engineering and Institute of Developmental Biology and Molecular Medicine at Fudan University for mouse husbandry and the Flow Cytometry Core Facility for FACS sorting and analysis. The authors acknowledge other members of the Yu laboratory and the Liu laboratory for technical assistance.

Funding was provided by the National Key Research and Development Program of China, 2021YFA0804703 (X. Yu); the Natural Science Foundation of Shanghai, 20ZR1472200 (X. Yu); the National Natural Science Foundation of China, 82172837 (Y. Liu); the Open Research Fund of National Key Laboratory of Immunity and Inflammation, JCKFKT-ZD-003 (X. Yu, Y. Liu); the China Postdoctoral Science Foundation, 2023M740698 (X. Li); and the Postdoctoral Fellowship Program of China Postdoctoral Science Foundation, GZC20230518 (X. Li).

Author contributions: X. Li: Funding acquisition, Investigation, Visualization, H. Yi: Investigation, Z. Jin: Investigation, Visualization, K. Jiang: Investigation, K. Xue: Investigation, J. Wang: Investigation, Y. Qian: Investigation, Q. Xiang: Investigation, S. Zhu: Investigation, R. Yan: Investigation, Y. Yang: Investigation, S. Sun: Methodology, K. Li: Investigation, Z. Zhou: Investigation, W. Yu: Resources, N. Jiang: Methodology, C. Ding: Methodology, X. Lin: Methodology, J. Zhong: Investigation, Y. Dong: Investigation, Y. Liu: Funding acquisition, Investigation, Visualization, Writing - original draft, Writing - review & editing, X. Yu: Conceptualization, Formal analysis, Funding acquisition, Project administration, Supervision, Visualization, Writing – original draft, Writing – review & editing.

Disclosures: The authors declare no competing interests exist.

Submitted: 4 June 2024
Revised: 19 September 2024
Accepted: 17 October 2024

References

Ascic, E., F. Åkerström, M. Sreekumar Nair, A. Rosa, I. Kurochkin, O. Zimmermannova, X. Catena, N. Rotankova, C. Veser, M. Rudnik, et al. 2024. In vivo dendritic cell reprogramming for cancer immunotherapy. *Science*. 386:eadn9083. https://doi.org/10.1126/science.adn9083

Balachandran, V.P., M. Luksza, J.N. Zhao, V. Makarov, J.A. Moral, R. Remark, B. Herbst, G. Askan, U. Bhanot, Y. Senbabaoglu, et al. 2017. Identification of unique neoantigen qualities in long-term survivors of pancreatic cancer. *Nature*. 551:512–516. https://doi.org/10.1038/nature24462

Burdziak, C., D. Alonso-Curbelo, T. Walle, J. Reyes, F.M. Barriga, D. Haviv, Y. Xie, Z. Zhao, C.J. Zhao, H.A. Chen, et al. 2023. Epigenetic plasticity cooperates with cell-cell interactions to direct pancreatic tumorigenesis. *Science*. 380:eadd5327. https://doi.org/10.1126/science.add5327

Chavez, A., J. Scheiman, S. Vora, B.W. Pruitt, M. Tuttle, E. P R Iyer, S. Lin, S. Kiani, C.D. Guzman, D.J. Wiegand, et al. 2015. Highly efficient Cas9-mediated transcriptional programming. *Nat. Methods*. 12:326–328. https://doi.org/10.1038/nmeth.3312

Chen, X., Q. Lu, H. Zhou, J. Liu, B. Nadorp, A. Lasry, Z. Sun, B. Lai, G. Rona, J. Zhang, et al. 2023. A membrane-associated MHC-I inhibitory axis for cancer immune evasion. *Cell*. 186:3903–3920.e21. https://doi.org/10.1016/j.cell.2023.07.016

Friedman, J.M. 2019. Leptin and the endocrine control of energy balance. *Nat. Metab.* 1:754–764. https://doi.org/10.1038/s42255-019-0095-y

Galon, J., and D. Bruni. 2019. Approaches to treat immune hot, altered and cold tumours with combination immunotherapies. *Nat. Rev. Drug Discov.* 18:197–218. https://doi.org/10.1038/s41573-018-0007-y

Gettinger, S., J. Choi, K. Hastings, A. Truini, I. Datar, R. Sowell, A. Wurtz, W. Dong, G. Cai, M.A. Melnick, et al. 2017. Impaired HLA class I antigen processing and presentation as a mechanism of acquired resistance to immune checkpoint inhibitors in lung cancer. *Cancer Discov.* 7:1420–1435. https://doi.org/10.1158/2159-8290.CD-17-0593

Gilbert, L.A., M.A. Horlbeck, B. Adamson, J.E. Villalta, Y. Chen, E.H. Whitehead, C. Guimaraes, B. Panning, H.L. Ploegh, M.C. Bassik, et al. 2014. Genome-scale CRISPR-mediated control of gene repression and activation. *Cell*. 159:647–661. https://doi.org/10.1016/j.cell.2014.09.029

Gotwals, P., S. Cameron, D. Cipolletta, V. Cremasco, A. Crystal, B. Hewes, B. Mueller, S. Quaratino, C. Sabatos-Peyton, L. Petruzzelli, et al. 2017. Prospects for combining targeted and conventional cancer therapy with immunotherapy. *Nat. Rev. Cancer*. 17:286–301. https://doi.org/10.1038/nrc.2017.17

Gourisankar, S., A. Krokhotin, W. Ji, X. Liu, C.Y. Chang, S.H. Kim, Z. Li, W. Wenderski, J.M. Simanauskaite, H. Yang, et al. 2023. Rewiring cancer drivers to activate apoptosis. *Nature*. 620:417–425. https://doi.org/10.1038/s41586-023-06348-2

Griffioen, M., I.J. Ouwerkerk, V. Harten, and P.I. Schrier. 2000. HLA-B locus-specific downregulation in human melanoma requires enhancer A as well as a sequence element located downstream of the transcription initiation site. *Immunogenetics*. 52:121–128. https://doi.org/10.1007/s002510000262

Hanahan, D., and R.A. Weinberg. 2011. Hallmarks of cancer: The next generation. *Cell*. 144:646–674. https://doi.org/10.1016/j.cell.2011.02.013

Ho, W.J., E.M. Jaffee, and L. Zheng. 2020. The tumour microenvironment in pancreatic cancer - clinical challenges and opportunities. *Nat. Rev. Clin. Oncol.* 17:527–540. https://doi.org/10.1038/s41571-020-0363-5

Horlbeck, M.A., L.A. Gilbert, J.E. Villalta, B. Adamson, R.A. Pak, Y. Chen, A.P. Fields, C.Y. Park, J.E. Corn, M. Kampmann, and J.S. Weissman. 2016. Compact and highly active next-generation libraries for CRISPR-mediated gene repression and activation. *Elife*. 5:e19760. https://doi.org/10.7554/eLife.19760

Huang, C.J., X. Lyu, and J. Kang. 2022. The molecular characteristics and functional roles of microspherule protein 1 (MCRS1) in gene expression, cell proliferation, and organismic development. *Cell Cycle*. 22:619–632. https://doi.org/10.1080/15384101.2022.2145816

Island, M.L., T. Mesplede, N. Darracq, M.T. Bandu, N. Christeff, P. Djian, J. Drouin, and S. Navarro. 2002. Repression by homeoprotein pitx1 of virus-induced interferon a promoters is mediated by physical interaction and trans repression of IRF3 and IRF7. *Mol. Cell. Biol.* 22:7120–7133. https://doi.org/10.1128/MCB.22.20.7120-7133.2002

Johnson, B.A. III, M. Yarchoan, V. Lee, D.A. Laheru, and E.M. Jaffee. 2017. Strategies for increasing pancreatic tumor immunogenicity. *Clin. Cancer Res.* 23:1656–1669. https://doi.org/10.1158/1078-0432.CCR-16-2318

Joung, J., P.C. Kirchgatterer, A. Singh, J.H. Cho, S.P. Nety, R.C. Larson, R.K. Macrae, R. Deasy, Y.Y. Tseng, M.V. Maus, and F. Zhang. 2022. CRISPR activation screen identifies BCL-2 proteins and B3GNT2 as drivers of cancer resistance to T cell-mediated cytotoxicity. *Nat. Commun.* 13:1606. https://doi.org/10.1038/s41467-022-29205-8

Joung, J., S. Ma, T. Tay, K.R. Geiger-Schuller, P.C. Kirchgatterer, V.K. Verdine, B. Guo, M.A. Arias-Garcia, W.E. Allen, A. Singh, et al. 2023. A transcription factor atlas of directed differentiation. *Cell*. 186:209–229.e26. https://doi.org/10.1016/j.cell.2022.11.026

Kabir, A.U., C. Zeng, M. Subramanian, J. Wu, M. Kim, K. Krchma, X. Wang, C.M. Halabi, H. Pan, S.A. Wickline, et al. 2024. ZBTB46 coordinates angiogenesis and immunity to control tumor outcome. *Nat. Immunol.* 25:1546–1554. https://doi.org/10.1038/s41590-024-01936-4

Kearney, C.J., S.J. Vervoort, S.J. Hogg, K.M. Ramsbottom, A.J. Freeman, N. Lalaoui, L. Pijpers, J. Michie, K.K. Brown, D.A. Knight, et al. 2018. Tumor immune evasion arises through loss of TNF sensitivity. *Sci. Immunol.* 3:eaar3451. https://doi.org/10.1126/sciimmunol.aar3451

Kidger, A.M., M.K. Saville, L.K. Rushworth, J. Davidson, J. Stellzig, M. Ono, L.A. Kuebelsbeck, K.P. Janssen, B. Holzmann, J.P. Morton, et al. 2022. Suppression of mutant Kirsten-RAS (KRAS(G12D))-driven pancreatic carcinogenesis by dual-specificity MAP kinase phosphatases 5 and 6. *Oncogene*. 41:2811–2823. https://doi.org/10.1038/s41388-022-02302-0

Kobayashi, K.S., and P.J. van den Elsen. 2012. NLRC5: A key regulator of MHC class I-dependent immune responses. *Nat. Rev. Immunol.* 12:813–820. https://doi.org/10.1038/nri3339

Li, J., K.T. Byrne, F. Yan, T. Yamazoe, Z. Chen, T. Baslan, L.P. Richman, J.H. Lin, Y.H. Sun, A.J. Rech, et al. 2018. Tumor cell-intrinsic factors underlie heterogeneity of immune cell infiltration and response to immunotherapy. *Immunity*. 49:178–193.e7. https://doi.org/10.1016/j.immuni.2018.06.006

Li, W., H. Xu, T. Xiao, L. Cong, M.I. Love, F. Zhang, R.A. Irizarry, J.S. Liu, M. Brown, and X.S. Liu. 2014. MAGeCK enables robust identification of essential genes from genome-scale CRISPR/Cas9 knockout screens. *Genome Biol.* 15:554. https://doi.org/10.1186/s13059-014-0554-4

Liao, G., J. Wang, J. Guo, J. Allard, J. Cheng, A. Ng, S. Shafer, A. Puech, J.D. McPherson, D. Foernzler, et al. 2004. In silico genetics: Identification of a functional element regulating H2-Ealpha gene expression. *Science*. 306:690–695. https://doi.org/10.1126/science.1100636

Liu, X., X. Bao, M. Hu, H. Chang, M. Jiao, J. Cheng, L. Xie, Q. Huang, F. Li, and C.Y. Li. 2020. Inhibition of PCSK9 potentiates immune checkpoint therapy for cancer. *Nature*. 588:693–698. https://doi.org/10.1038/s41586-020-2911-7

Liu, Y., Y. Gu, Y. Han, Q. Zhang, Z. Jiang, X. Zhang, B. Huang, X. Xu, J. Zheng, and X. Cao. 2016. Tumor exosomal RNAs promote lung pre-metastatic niche formation by activating alveolar epithelial TLR3 to recruit neutrophils. *Cancer Cell*. 30:243–256. https://doi.org/10.1016/j.ccell.2016.06.021

Lu, Y.H., O.S. Dallner, K. Birsoy, G. Fayzikhodjaeva, and J.M. Friedman. 2015. Nuclear Factor-Y is an adipogenic factor that regulates leptin gene expression. *Mol. Metab.* 4:392–405. https://doi.org/10.1016/j.molmet.2015.02.002

Łuksza, M., Z.M. Sethna, L.A. Rojas, J. Lihm, B. Bravi, Y. Elhanati, K. Soares, M. Amisaki, A. Dobrin, D. Hoyos, et al. 2022. Neoantigen quality predicts immunoediting in survivors of pancreatic cancer. *Nature*. 606:389–395. https://doi.org/10.1038/s41586-022-04735-9

Maleki Vareki, S. 2018. High and low mutational burden tumors versus immunologically hot and cold tumors and response to immune checkpoint inhibitors. *J. Immunother. Cancer*. 6:157. https://doi.org/10.1186/s40425-018-0479-7

Mellman, I., D.S. Chen, T. Powles, and S.J. Turley. 2023. The cancer-immunity cycle: Indication, genotype, and immunotype. *Immunity*. 56:2188–2205. https://doi.org/10.1016/j.immuni.2023.09.011

Mellman, I., G. Coukos, and G. Dranoff. 2011. Cancer immunotherapy comes of age. *Nature*. 480:480–489. https://doi.org/10.1038/nature10673

Metcalf, K.J., A. Alazzeh, Z. Werb, and V.M. Weaver. 2021. Leveraging microenvironmental synthetic lethalities to treat cancer. *J. Clin. Invest.* 131:eJCI143765. https://doi.org/10.1172/JCI143765

Newman, A.M., C.B. Steen, C.L. Liu, A.J. Gentles, A.A. Chaudhuri, F. Scherer, M.S. Khodadoust, M.S. Esfahani, B.A. Luca, D. Steiner, et al. 2019. Determining cell type abundance and expression from bulk tissues with digital cytometry. *Nat. Biotechnol.* 37:773–782. https://doi.org/10.1038/s41587-019-0114-2

Overwijk, W.W., A. Tsung, K.R. Irvine, M.R. Parkhurst, T.J. Goletz, K. Tsung, M.W. Carroll, C. Liu, B. Moss, S.A. Rosenberg, and N.P. Restifo. 1998. gp100/pmel 17 is a murine tumor rejection antigen: induction of "self"-reactive, tumoricidal T cells using high-affinity, altered peptide ligand. *J. Exp. Med.* 188:277–286. https://doi.org/10.1084/jem.188.2.277

Parker, B.S., J. Rautela, and P.J. Hertzog. 2016. Antitumour actions of interferons: Implications for cancer therapy. *Nat. Rev. Cancer*. 16:131–144. https://doi.org/10.1038/nrc.2016.14

Patel, S.J., N.E. Sanjana, R.J. Kishton, A. Eidizadeh, S.K. Vodnala, M. Cam, J.J. Gartner, L. Jia, S.M. Steinberg, T.N. Yamamoto, et al. 2017. Identification of essential genes for cancer immunotherapy. *Nature*. 548:537–542. https://doi.org/10.1038/nature23477

Pishesha, N., T.J. Harmand, and H.L. Ploegh. 2022. A guide to antigen processing and presentation. *Nat. Rev. Immunol.* 22:751–764. https://doi.org/10.1038/s41577-022-00707-2

Pommier, A., N. Anaparthy, N. Memos, Z.L. Kelley, A. Gouronnec, R. Yan, C. Auffray, J. Albrengues, M. Egeblad, C.A. Iacobuzio-Donahue, et al. 2018. Unresolved endoplasmic reticulum stress engenders immune-resistant, latent pancreatic cancer metastases. *Science*. 360:eaao4908. https://doi.org/10.1126/science.aao4908

Rotzschke, O., K. Falk, S. Stevanovic, G. Jung, P. Walden, and H.G. Rammensee. 1991. Exact prediction of a natural T cell epitope. *Eur. J. Immunol.* 21:2891–2894. https://doi.org/10.1002/eji.1830211136

Runge, J.S., J.R. Raab, and T. Magnuson. 2018. Identification of two distinct classes of the human INO80 complex genome-wide. *G3 (Bethesda)*. 8:1095–1102. https://doi.org/10.1534/g3.117.300504

Schumacher, T.N., and R.D. Schreiber. 2015. Neoantigens in cancer immunotherapy. *Science*. 348:69–74. https://doi.org/10.1126/science.aaa4971

Siegel, R.L., K.D. Miller, H.E. Fuchs, and A. Jemal. 2022. Cancer statistics, 2022. *CA Cancer J. Clin.* 72:7–33. https://doi.org/10.3322/caac.21708

Singer, M., C. Wang, L. Cong, N.D. Marjanovic, M.S. Kowalczyk, H. Zhang, J. Nyman, K. Sakuishi, S. Kurtulus, D. Gennert, et al. 2016. A distinct gene module for dysfunction uncoupled from activation in tumor-infiltrating T cells. *Cell*. 166:1500–1511 e1509. https://doi.org/10.1016/j.cell.2016.08.052

Stoeckius, M., S. Zheng, B. Houck-Loomis, S. Hao, B.Z. Yeung, W.M. Mauck III, P. Smibert, and R. Satija. 2018. Cell Hashing with barcoded antibodies enables multiplexing and doublet detection for single cell genomics. *Genome Biol.* 19:224. https://doi.org/10.1186/s13059-018-1603-1

Waldman, A.D., J.M. Fritz, and M.J. Lenardo. 2020. A guide to cancer immunotherapy: from T cell basic science to clinical practice. *Nat. Rev. Immunol.* 20:651–668. https://doi.org/10.1038/s41577-020-0306-5

Wang, L., C. Lynch, S.P. Pitroda, A. Piffko, K. Yang, A.K. Huser, H.L. Liang, and R.R. Weichselbaum. 2024. Radiotherapy and immunology. *J. Exp. Med.* 221:e20232101. https://doi.org/10.1084/jem.20232101

Weintraub, A.S., C.H. Li, A.V. Zamudio, A.A. Sigova, N.M. Hannett, D.S. Day, B.J. Abraham, M.A. Cohen, B. Nabet, D.L. Buckley, et al. 2017. YY1 is a structural regulator of enhancer-promoter loops. *Cell*. 171:1573–1588.e1528. https://doi.org/10.1016/j.cell.2017.11.008

Yamamoto, K., A. Venida, R.M. Perera, and A.C. Kimmelman. 2020a. Selective autophagy of MHC-I promotes immune evasion of pancreatic cancer. *Autophagy*. 16:1524–1525. https://doi.org/10.1080/15548627.2020.1769973

Yamamoto, K., A. Venida, J. Yano, D.E. Biancur, M. Kakiuchi, S. Gupta, A.S.W. Sohn, S. Mukhopadhyay, E.Y. Lin, S.J. Parker, et al. 2020b. Autophagy promotes immune evasion of pancreatic cancer by degrading MHC-I. *Nature*. 581:100–105. https://doi.org/10.1038/s41586-020-2229-5

Zhang, J.J., Y. Zhu, K.L. Xie, Y.P. Peng, J.Q. Tao, J. Tang, Z. Li, Z.K. Xu, C.C. Dai, Z.Y. Qian, et al. 2014. Yin Yang-1 suppresses invasion and metastasis of pancreatic ductal adenocarcinoma by downregulating MMP10 in a MUC4/ErbB2/p38/MEF2C-dependent mechanism. *Mol. Cancer*. 13:130. https://doi.org/10.1186/1476-4598-13-130

Zhang, J.J., Y. Zhu, X.F. Zhang, D.F. Liu, Y. Wang, C. Yang, G.D. Shi, Y.P. Peng, K. Zhang, L. Tian, et al. 2017. Yin Yang-1 suppresses pancreatic ductal adenocarcinoma cell proliferation and tumor growth by regulating SOX2OT-SOX2 axis. *Cancer Lett.* 408:144–154. https://doi.org/10.1016/j.canlet.2017.08.032

Zhong, W., J.S. Myers, F. Wang, K. Wang, J. Lucas, E. Rosfjord, J. Lucas, A.T. Hooper, S. Yang, L.A. Lemon, et al. 2020. Comparison of the molecular and cellular phenotypes of common mouse syngeneic models with human tumors. *BMC Genomics*. 21:2. https://doi.org/10.1186/s12864-019-6344-3

Supplemental material

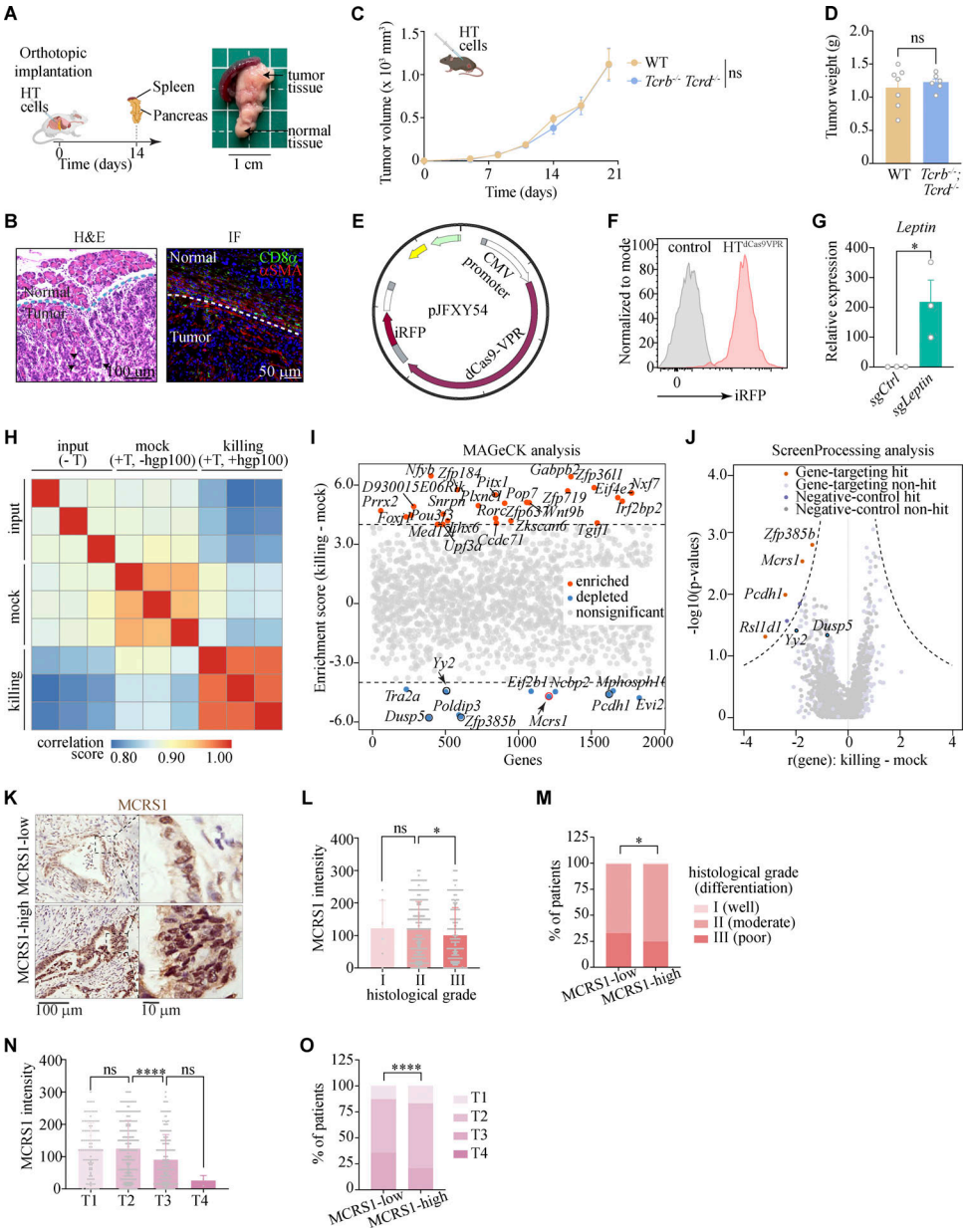

Figure S1. **CRISPRa screening identifies *Mcrs1* as a candidate immune-sensitizing factor. (A)** Orthotopic tumor formation by implanting HT cells into the mouse pancreas. Arrows point to the tumor and normal tissues (N = 2 independent experiments). Scale bar = 1 cm. Illustration was created with https://BioRender.com with modifications. **(B)** Orthotopic HT tumors exhibiting clinical features, assessed by H&E staining and immunofluorescence (IF) staining of αSMA (red, stroma) and CD8α (green, T cells) (n = 6 for both groups). Scale bar in the left panel = 100 μm, scale bar in the right panel = 50 μm. **(C)** Tumor growth of HT cells subcutaneously inoculated in *Tcrb*$^{-/-}$ *Tcrd*$^{-/-}$ mice, with WT mice obtained from SLAC as control (n = 7, 6 for WT and *Tcrb*$^{-/-}$ *Tcrd*$^{-/-}$ mice, respectively; presented as means ± SEM; ns, not significant, P ≥ 0.05; two-way ANOVA; N = 2 independent experiments). Illustration was created with https://BioRender.com. **(D)** Tumor weights in WT and *Tcrb*$^{-/-}$ *Tcrd*$^{-/-}$ mice at the point of sacrifice (n = 7, 6 for WT and *Tcrb*$^{-/-}$ *Tcrd*$^{-/-}$ mice, respectively; presented as means ± SEM; ns, not significant, P ≥ 0.05; two-tailed unpaired t test; N = 2 independent experiments). **(E)** Vector design to express *dCas9-VPR* in the HT cell line, which allows bicistronic expression of *dCas9-VPR* and *iRFP* via an Internal Ribosome Entry Site element. Illustration was created with SnapGene. **(F)** Flow cytometry analysis of iRFP expression in HT^{dCas9VPR} cells (N = 2 independent experiments). **(G)** CRISPRa activation of *Leptin* expression by *Leptin*-targeting sgRNAs in HT^{dCas9VPR} cells (n = 3 for both groups; presented as means ± SEM; *, P < 0.05; two-tailed unpaired t test; N = 2 independent experiments). **(H)** Correlation of sgRNA profiles in the input, mock, and T cell–killing samples of CRISPRa screening (n = 3 for all groups). **(I)** MAGeCK analysis of CRISPRa screening. **(J)** ScreenProcessing analysis of CRISPRa screening. **(K)** Representative immunohistochemistry images showing high and low expression of MCRS1 (brown) in clinical samples of human PDAC patients (n = 350, 354 for MCRS1-low and MCRS1-high groups, respectively). Scale bar in the left panel = 100 μm, scale bar for the right panel = 10 μm. **(L)** Expression of MCRS1 in PDAC samples of different histological grades determined by IHC (n = 7, 496, 201 for Grade I, Grade II, and Grade III, respectively; presented as means ± SD; ns, not significant, P ≥ 0.05; *, P < 0.05; two-tailed unpaired t test). **(M)** Histological grades of PDAC patients with high and low MCRS1 levels (n = 350, 354 for MCRS1-low and MCRS1-high groups, respectively; *, P < 0.05; Chi-square test). **(N)** Expression of MCRS1 in PDAC samples of different T stages (n = 105, 402, 194, 40 for T1, T2, T3, and T4, respectively; presented as means ± SD; ns, not significant, P ≥ 0.05; ****, P < 0.0001; two-tailed unpaired t test). **(O)** T stages of PDAC patients with high and low MCRS1 levels (n = 350, 354 for MCRS1-low and MCRS1-high groups, respectively; ****, P < 0.0001; Chi-square test).

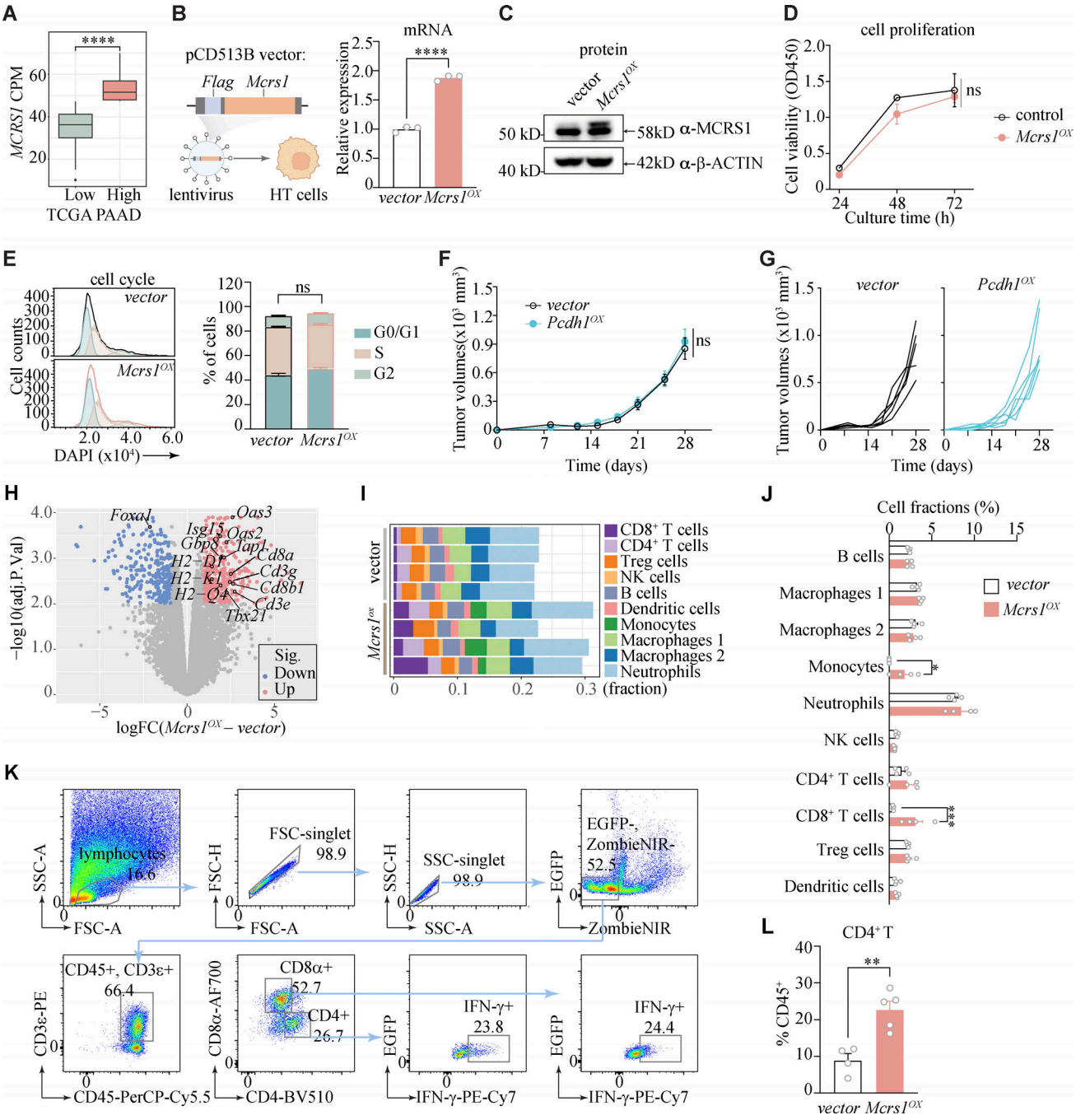

Figure S2. ***Mcrs1* activates T cell–mediated anti-tumor immunity in vivo. (A)** Expression of *MCRS1* in the *MCRS1*-low and *MCRS1*-high groups of PAAD patients in TCGA (n = 151, 30 for the *MCRS1*-low and *MCRS1*-high groups, respectively; center line, median; box limits, upper and lower quartiles; whiskers, Tukey; points, outliers; ****, P < 0.0001; two-tailed unpaired test). **(B)** Increased *Mcrs1* expression in HT cells by lentiviral transduction of the *Mcrs1* ORF (n = 3 for both groups; presented as means ± SEM; ****, P < 0.0001; two-tailed unpaired t test; N = 3 independent experiments). **(C)** Elevated MCRS1 protein levels in *Mcrs1*-overexpressing (*Mcrs1*^{OX}) cells (N = 3 independent experiments). **(D)** The proliferation of *Mcrs1*^{OX} and vector control cells in vitro, measured with the CCK-8 assay (n = 3 for both groups; presented as means ± SEM; ns, not significant, P ≥ 0.05; two-way ANOVA; N = 2 independent experiments). **(E)** Cell cycle analysis of *Mcrs1*^{OX} and vector control cells by flow cytometry, with representative histograms (left panel) and quantification (right panel) shown (n = 4 for both groups; presented as means ± SEM; ns, not significant, P ≥ 0.05; two-way ANOVA; N = 2 independent experiments). **(F)** Growth curve of subcutaneous *Pcdh1*^{OX} and vector control tumors in WT mice (n = 5, 6 for control and *Pcdh1*^{OX}, respectively; presented as means ± SEM; ns, not significant, P ≥ 0.05; two-way ANOVA; N = 2 independent experiments). **(G)** Spider plots showing tumor growth in individual mice as in F (N = 2 independent experiments). **(H)** Volcano plot showing differential gene expression between *Mcrs1*^{OX} and vector control tumors (n = 4 for both groups). **(I)** Fractions of different immune cell populations in *Mcrs1*^{OX} and vector control tumors estimated by CIBERSORTx. **(J)** Comparison of CIBERSORTx-estimated immune cell populations in *Mcrs1*^{OX} and vector control tumors (n = 4 for both groups; presented as means ± SEM; *, P < 0.05; ***, P < 0.001; two-tailed unpaired t test). **(K)** The gating strategy for T cell analysis in subcutaneous tumors. **(L)** Flow cytometry analysis of CD4⁺ T cells in *Mcrs1*^{OX} or vector control tumors (n = 4, 5 for vector control and *Mcrs1*^{OX}, respectively; presented as means ± SEM; **, P < 0.01; two-tailed unpaired t test; N > 3 independent experiments). Source data are available for this figure: SourceData FS2.

https://doi.org/10.1084/jem.20240959

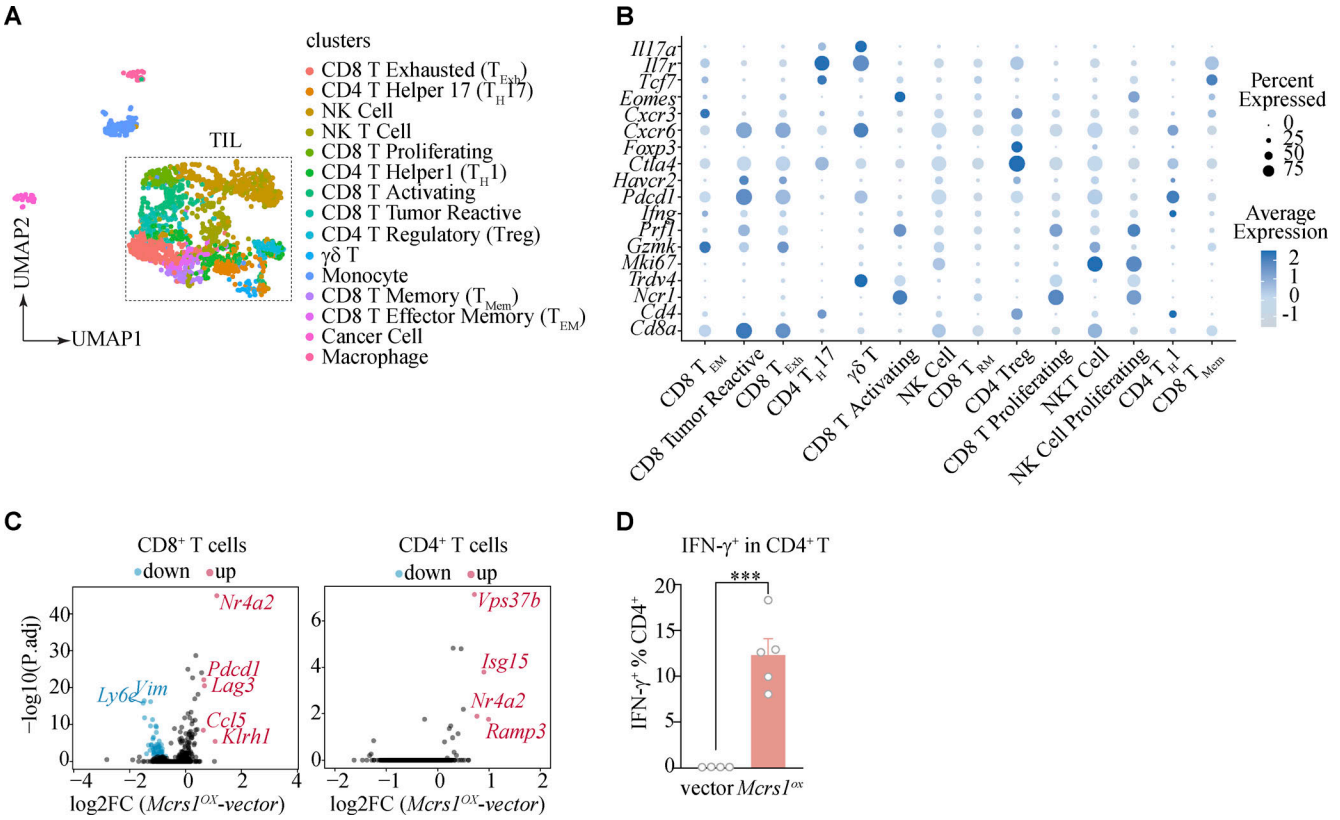

Figure S3. **scRNA-seq analysis of T cells in *Mcrs1*^{OX} and vector control tumors. (A)** UMAP embedding of all cell clusters captured by scRNA-seq analysis (n = 3 pooled for both groups). **(B)** Marker gene expression of different clusters of tumor-infiltrating lymphocytes. **(C)** Pseudo-bulk analysis of CD8⁺ and CD4⁺ T cells in *Mcrs1*^{OX} and vector control tumors, showing upregulation of activation markers in both subsets. **(D)** Flow cytometry analysis of IFN-γ⁺ effector CD4⁺ T cells in *Mcrs1*^{OX} and vector control tumors (n = 4, 5 for vector control and *Mcrs1*^{OX}, respectively; presented as means ± SEM; ***, P < 0.001; two-tailed unpaired t test; N > 3 independent experiments).

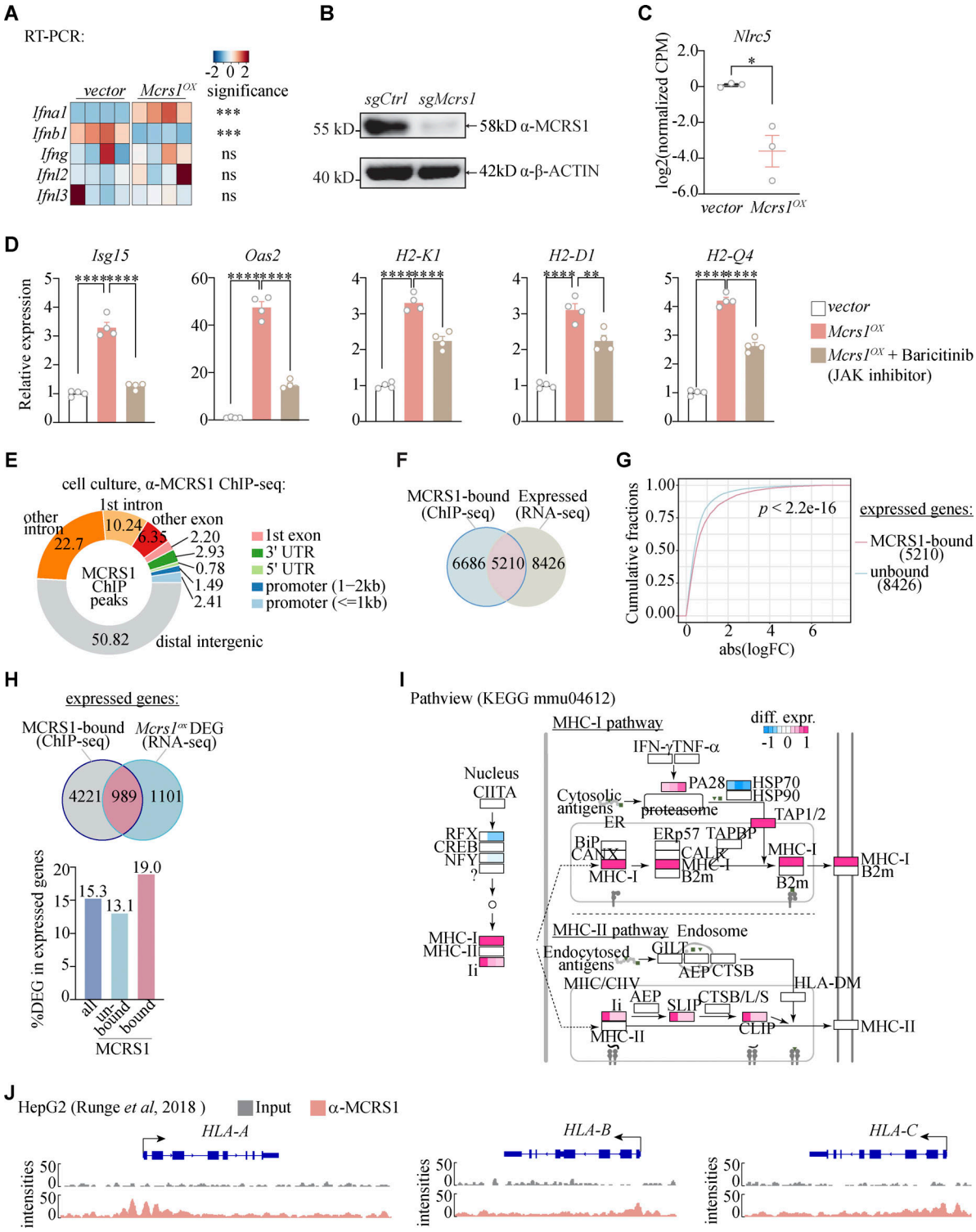

Figure S4. **MCRS1 regulates MHC-I expression by directly binding to the promoters. (A)** Expression of interferons in *Mcrs1*^{OX} and vector control cells (n = 4 for both groups; ns, not significant, P ≥ 0.05; ***, P < 0.001; two-tailed unpaired t test; N = 2 independent experiments). **(B)** *Mcrs1* knockout confirmed by western blotting, representative images shown (N = 3 independent experiments). **(C)** *Nlrc5* expression in *Mcrs1*^{OX} and vector control cells determined by RNA-seq (n = 3 for both groups; presented as means ± SEM; *, P < 0.05; two-tailed unpaired t test). **(D)** Expression of ISGs and MHC-I genes in *Mcrs1*^{OX} cells in the presence of a JAK inhibitor (n = 4 for all groups; presented as means ± SEM; **, P < 0.01; ****, P < 0.0001; one-way ANOVA with Tukey's multiple comparisons test; N = 2 independent experiments). **(E)** Distribution of MCRS1 ChIP peaks across the genome. **(F)** Overlapping of MCRS1-bound and expressed genes in HT cells. **(G)** The cumulative distribution function (CDF) plot of absolute expression changes of MCRS1-bound and -unbound genes in *Mcrs1*^{OX} and vector control cells. **(H)** Percentages of differentially expressed genes (DEG) in MCRS1-bound and -unbound genes. **(I)** Pathview analysis of differential expression of MCRS1-bound genes in the antigen presentation pathway in control and *Mcrs1*^{OX} cells. **(J)** MCRS1 binding at the human MHC-I loci (*HLA-A/B/C*) in HepG2 cells (Runge et al., 2018). Source data are available for this figure: SourceData FS4.

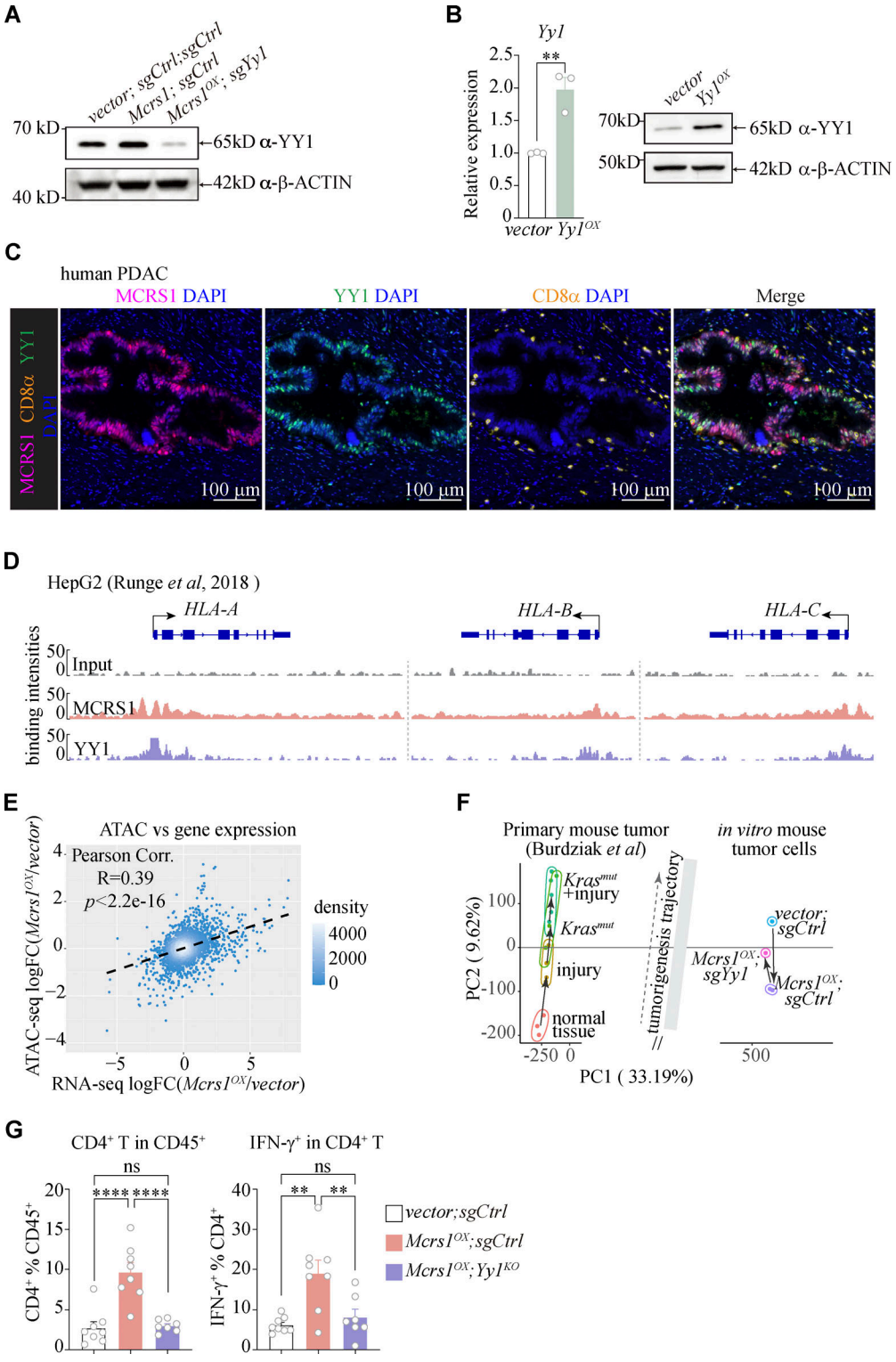

Figure S5. **MCRS1 regulates MHC-I through YY1. (A)** YY1 protein levels in control, *Mcrs1*^{OX}, and *Mcrs1*^{OX}*;sgYy1* tumors (N = 2 independent experiments). **(B)** Overexpression of *Yy1* was confirmed at the mRNA and protein levels (n = 3 for both groups in qPCR; presented as means ± SEM; **, P < 0.01; two-tailed unpaired t test; N = 2 independent experiments). **(C)** Representative images of immunofluorescence staining of DAPI (blue, DNA), MCRS1 (magenta), YY1 (green), and CD8α (orange, T cell) in human PDAC samples. Scale bars = 100 μm. **(D)** Binding of MCRS1 and YY1 at the human MHC-I loci (*HLA-A/B/C*) in HepG2 cells. **(E)** Correlation between the changes of ATAC-seq signals and the changes of gene expression in control and *Mcrs1*^{OX} cells. FC, fold change. **(F)** Integrative analysis of ATAC-seq profiles of *vector;sgCtrl*, *Mcrs1*^{OX}*;sgCtrl*, and *Mcrs1*^{OX}*;sgYy1* cells, compared to the tumor development trajectory defined by ATAC-seq profiles of mouse primary pancreatic cancer at different tumorigenesis stages (Burdziak et al., 2023). **(G)** Total and effector CD4$^+$ T cells in *vector;sgCtrl*, *Mcrs1*^{OX}*;sgCtrl*, and *Mcrs1*^{OX}*;sgYy1* tumors (n = 8, 8, 7; presented as means ± SEM; ns, not significant, P ≥ 0.05; **, P < 0.01; ****, P < 0.0001; one-way ANOVA with Tukey's multiple comparisons test; N = 3 independent experiments). Source data are available for this figure: SourceData FS5.

Provided online are Table S1, Table S2, Table S3, Table S4, Table S5, and Table S6. Table S1 shows PDAC patient information in histological studies. Table S2 shows overlapping genes between RNA-seq, ChIP-seq, and ATAC-seq. Table S3 shows PDAC patient information in the NAC study. Table S4 shows NSCLC patient information in the anti-PD1 immunotherapy study. Table S5 shows primers used in the study. Table S6 shows sgRNAs used in the study.